



**HAL**  
open science

# Optimal Design of a Multipole-Electromagnet Robotic Platform for Ophthalmic Surgery

Ruipeng Chen, David Folio, Antoine Ferreira

► **To cite this version:**

Ruipeng Chen, David Folio, Antoine Ferreira. Optimal Design of a Multipole-Electromagnet Robotic Platform for Ophthalmic Surgery. *Micromachines*, 2022, Special Issue Recent Advances in Micro-robotics, 14 (1), pp.91. 10.3390/mi14010091 . hal-03919809

**HAL Id: hal-03919809**

**<https://hal.science/hal-03919809>**

Submitted on 5 Apr 2024

**HAL** is a multi-disciplinary open access archive for the deposit and dissemination of scientific research documents, whether they are published or not. The documents may come from teaching and research institutions in France or abroad, or from public or private research centers.

L'archive ouverte pluridisciplinaire **HAL**, est destinée au dépôt et à la diffusion de documents scientifiques de niveau recherche, publiés ou non, émanant des établissements d'enseignement et de recherche français ou étrangers, des laboratoires publics ou privés.



Distributed under a Creative Commons Attribution 4.0 International License

# Optimal Design of a Multipole Electromagnets Robotic Platform for the Ophthalmic Surgery

Ruipeng Chen <sup>1,†,‡</sup> , David Folio <sup>†,‡,\*</sup>  and Antoine Ferreira <sup>†,‡,\*</sup> 

<sup>1</sup> Ruipeng.Chen@INSA-CVL.FR; INSA Centre Val de Loire.

\* Correspondences: David Folio: David.Folio@INSA-CVL.FR, Tel: +33 (0)2 48 48 40 75;  
Antoine Ferreira: Antoine.Ferreira@INSA-CVL.FR, Tel: +33 (0)2 48 48 40 79.

† Current address: INSA Centre Val de Loire, 88 Boulevard Lahitolle, 18000 Bourges, France

‡ These authors contributed equally to this work.

**Abstract:** The aim of this paper is to design a multipole electromagnet robotic platform named OctoRob. This platform provides a minimally invasive means for targeted therapeutic interventions in specific intraocular areas. The proposed OctoRob is capable of generating both appropriate magnetic fields and gradients. The main scientific objectives are: i) To propose an optimal reconfigurable arrangement of electromagnets suitable for ophthalmic interventions. ii) To model, design and implement a one-degree-of-freedom robotic arm connected with an electromagnet in order to optimize the generation of magnetic fields and gradients. iii) To evaluate the magnetic performances of the OctoRob platform including different tilted angles. The results show that the OctoRob platform has great potential to be applied for the ophthalmic surgery.

**Keywords:** Electromagnetic actuation system; Microrobotic surgery platform; Ophthalmic surgery; Optimization of magnetic systems; Microrobots

## 1. Introduction

Biomedical magnetic microrobots provide a promising alternative approach for many clinical procedures [1]. To this aim, a reliable and effective electromagnetic actuation (EMA) setup should be designed with respect to the medical applications objectives. In previous researches [2,3], the magnetic source generation, the minimum number of electromagnets for an EMA system and the optimization methodology for the configuration of electromagnets have been fully studied for different common applications. This previous work showed that the EMA optimal design is strongly related to the considered application. In particular, most EMA arrangements, such as OctoMag-like or MiniMag-like [4], exhibit different magnetic performance for different coil positions and orientations [2]. However, with a fixed configuration of their coils, OctoMag or MiniMag cannot be easily adapted to different application contexts. Therefore, here, we focus on the optimization and implementation of an EMA platform using the methodology proposed in [3] with the initial motivation of being applied to ophthalmic minimally invasive surgery (MIS) using medical magnetic microrobots that have to achieve various tasks. Through the theoretical analysis of the system design, a robotic microrobotic EMA platform, named OctoRob, with a re-configurable setting is developed.

Many retinal procedures was limited by human performance and perception [5–7]. The manipulation of retinal membranes is very delicate, and safe interaction requires forces at best of the order of what the surgeon can receive [5]. The use of microrobots will mitigate traction on the retina with potentiality to circumvent the necessity to remove some vitreous humor (i.e. perform a vitrectomy) from the eye [4,8–11]. Figure 1 illustrates the classical anatomy of the Human eye. It can navigate in the eye cavity and then perform ophthalmic MIS tasks (such as material removal, drug delivery, punctures...), that thus has the great potential to revolutionize the eye therapy and improve the patient care and recovery. Specifically, biomedical microrobot can be injected in the retina through a small incision, and controlled by manipulating the applied magnetic fields and gradients induced from the developed OctoRob platform, as depicted in Figure 2. OctoRob should



**Citation:** Ruipeng, C.; David, F.; Antoine, F. Optimal design of a multipole electromagnets robotic platform for the ophthalmic surgery. *Preprints* **2022**, *1*, 0. <https://doi.org/10.3390/mi14010091>

**Publisher's Note:** MDPI stays neutral with regard to jurisdictional claims in published maps and institutional affiliations.



**Copyright:** © 2022 by the authors. Licensee MDPI, Basel, Switzerland. This article is an open access article distributed under the terms and conditions of the Creative Commons Attribution (CC BY) license (<https://creativecommons.org/licenses/by/4.0/>).

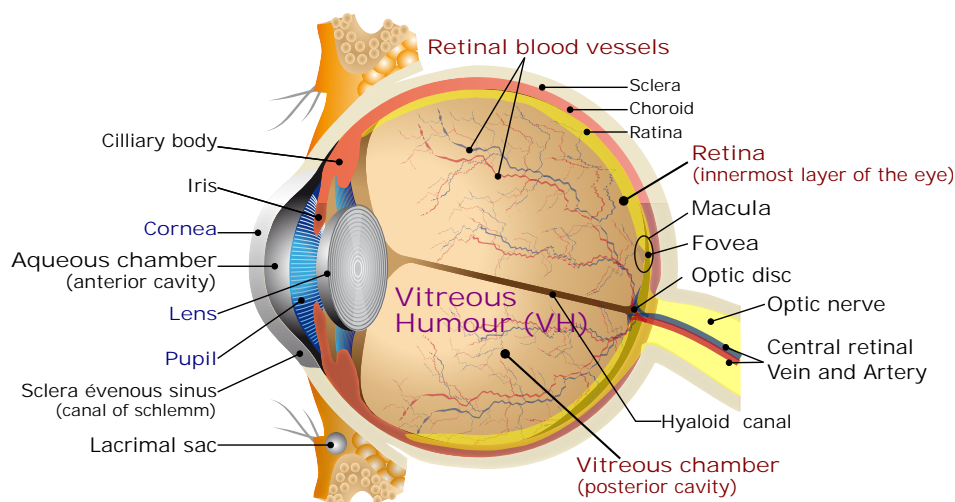


**Figure 1.** Schematic representation of the Human eye.

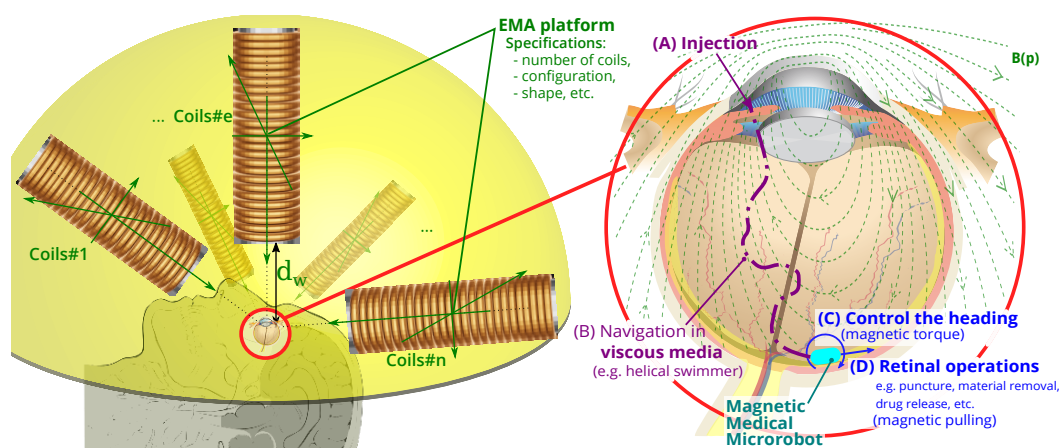


**Figure 2.** Illustration of the ophthalmic microrobotic MIS system: (left) the EMA platform that should respect the geometry of the human head, that is arranged in the yellow hemisphere; (right) the ophthalmic microrobotic MIS procedure where biomedical mirorobot is injected by surgeon and controlled by the EMA setup; the generated magnetic field and gradient induce the magnetic torque and pulling force to the medical microrobot for the different steps of the operations.

be designed accordingly to manipulate efficiently the untethered microrobot with full dexterity. In particular, the biomedical microrobot would have to navigate in the mostly gel-like medium of the vitreous humor (VH). Under such physiological condition, the helical microswimmer is known to be the most efficient propulsion mechanism and thus need proper magnetic field [12–17]. Then, magnetic force would be required to perform the therapeutic tasks (e.g. puncture, peeling, etc.) and thus need proper magnetic gradient field. Therefore, generating the appropriate magnetic fields and gradients distribution from the considered OctoRob setup is important issue that must be investigated with regard to the specific biomedical application.

This paper is devoted to the study of the modeling, design and optimization of appropriate magnetic robotic platform to provide more effective magnetic fields and gradients on microrobots for performing the given medical tasks, that is, here, an ophthalmic MIS intervention. To this aim, the paper is organized as follows. Ophthalmology and ophthalmic surgery challenges and opportunities are first discussed and the requirements of the considered application are thereby specified. The overall concept of the designed EMA system is represented according to the given specifications stated in [3,18]. The set of electromagnetic coil is firstly investigated, including its magnetic core and its optimal dimensions. Then, the designed coil is evaluated and implemented. Furthermore, a suitable

design of the robotic arm is applied. The kinematic mechanism is then analyzed. The robotic arm is integrated in order to optimize the performance of dexterity of magnetic fields and gradients as introduced in [2,3]. Finally, the designed prototype is built from the ophthalmic application specifications. The magnetic capability of OctoRob are evaluated to characterize its capability of inducing either good magnetic fields or good gradients.

## 2. Ophthalmic Surgery Specifications

Ophthalmology is the branch of medicine that is concerned with the eye and its diseases. There exists a number of textbooks with in-depth analysis of the eye such as the work by Snell and Lemp [19]. Similarly, there are numerous conditions of the eye that all require their specific forms of treatments. In particular, the discipline of vitreoretinal surgery includes basically all operations related to the vitreous and to the delicate retina (see also the Figure 1), whose health is essential for a good vision. Such ophthalmic procedures have great potential to be performed involving less invasiveness through medical intraocular magnetic microrobots. Retinal surgery requires extremely precise movements and small tool/tissue interaction forces. Otherwise, there is a potential risk of permanent damage (i.e. permanent vision loss) through even small surgeon error. For instance, one particularly difficult procedure is the retinal vein cannulation to alleviate its occlusion. Such retinal occlusion is one of the most common causes of vision loss to patients, with a prevalence of 1.6% for adults aged 49 years or older [20]. Various treatment methods for this pathology have been proposed. For instance, intravitreal thrombolysis<sup>1</sup> with tissue plasminogen activator injection is the most promising treatment [21]. To do so, thrombolytic enzyme (i.e. clot-busting) has to be injected into the tiny occluded vein (diameter of about 100  $\mu\text{m}$ ). Another challenging procedure is the peeling of epiretinal membranes (also called macular pucker). This disease of the eye makes a change in the VH leading to distortions of the vision, and its contraction can lead to severe vision impairment. The formation of such scar tissue on the retina can have a variety of reasons like age, trauma, idiopathic cause, etc. In order to remove such membrane, surgeon can peel it off with a micro-forceps. All these retinal procedures involve accurate positioning and force sensing that are at or beyond the sensation and control ability of most surgeons [5-7]. For instance, Gupta *et al.* [5] determined that only approximately 20% of contact events between the surgical tool and the retinal tissue during retinal microsurgery can be felt by the practitioner. This implies that most ophthalmic procedures are likely performed without haptic feedback and the surgeon relies mainly on visual tissue interaction. This lack of haptic feedback could adversely affect surgical outcome, as previous studies have shown that using only visual feedback increases the duration of manual manipulation tasks and reduces precision. Roughly 75% of all forces measured during retinal microsurgery were found to be less than 7.5 mN [5]. Although the forces in the study of Jagtap and Riviere [6] are somewhat higher, there is still substantial evidence that the forces involved during retinal surgery are at or beyond the limits of human perception.

In addition to its complexity, conventional vitreoretinal surgery is an invasive process. During the intervention different tools are placed in the eye, such as an irrigation line to maintain constant pressure, a light source to improve the visibility, and the required surgical instrument to perform the desired task [22]. Furthermore, most procedures that are performed on the retina require a preliminary *vitreotomy* (i.e. removing some VH) to be able to target the actual disease site. Nevertheless, performing vitreotomy is an arduous procedure that requires extreme care. Moreover, the performance is hampered because it is difficult to determine the VH that needs to be removed. Additionally, there is a high risk of complications after the procedure.

Due to the difficulty of accessing to the delicate retina during the MIS procedures, vitreoretinal surgery could be rendered less invasive and safer through the use of intraocular magnetic microrobots. In comparison to larger tools, the small size of such therapeutic

<sup>1</sup> Thrombolysis, also called fibrinolytic therapy, is the breakdown of blood clots formed in blood vessels.

agents will mitigate traction on the retina with the potential to completely circumvent the necessity to perform a vitrectomy to access the retina. With the goal of enabling less invasiveness and safer retinal operations, as well as providing an increased level of dexterity desired by clinicians, the designed EMA platform is considered for the magnetic manipulation of a fully untethered and dexterous microrobotic device inside the volume of a human eye.

### 2.1. Ophthalmic Microrobotic MIS

Even the most skilled surgeons have involuntary physiological tremors, which causes most ophthalmic surgeries at the peak of human capabilities [5–7]. To improve the surgeon's performance, different robotics technologies have been involved [4,8–11]. Although most of these current robotic solutions improve the quality of ophthalmic surgery, the invasiveness of the procedure is not fully reduced. The use of untethered magnetic microrobot is a promising alternative to enhance the overall ophthalmic MIS operations.

There is a wide variety of solutions and techniques to magnetically actuate a medical microrobot. The choice of the proper magnetic microrobotic system should be defined with respect to the biomedical application, here for an ophthalmic MIS procedure. The envisioned microrobotic MIS system for eye intervention is shown in Figure 2. First, magnetic microrobot is injected by the operator through a tiny incision to potentially circumvent the necessity of performing a vitrectomy. The biomedical microrobot consists of magnetic material and can be controlled through the applied magnetic field. Next, the magnetic microrobot is actuated to navigate in the VH that fills the space between the lens and the retina (see also Figure 1). Its workspace is basically filled by a transparent gel-like steady medium with a non-Newtonian rheological property [23–25]. In details, the VH is composed of about  $\sim 99\%$  water with the addition of  $\sim 0.9\%$  salts, and  $\sim 0.1\%$  of a network of collagen<sup>2</sup> fibrils and hyaluronan<sup>3</sup> that all form a scaffolding [25]. The collagen concentration in VH is around  $40 \mu\text{g cm}^{-3}$  to  $120 \mu\text{g cm}^{-3}$ , and collagen type II is the most abundant type in the eye. This presence of collagen leads to a gelatinous consistency, and thus the VH has a viscosity 2–4 times greater than of water ( $\rho_{\text{water}} = 1 \text{ mPa s}$ ) To perform the specified medical tasks, the microrobot must be capable of moving efficiently and reliably in the 3D workspace of the eyeball. Typically, microrobot is manipulated in fluids at the low-Reynolds-number regime (e.g.  $Re \ll 1$ ), where viscous drag significantly dominates over inertia [26]. In such physiological condition, helical microswimmer is known to be one of the most efficient propulsion mechanism [12–17].

On the other hand, the microrobot is positioned and oriented on the targeted site and then performs the specified ophthalmic tasks, such as targeted therapy and/or material removal (peeling, puncture, drug delivery, etc.). For instance, to perform a lamina puncture for the treatment of retinal vein occlusion, the biomedical microrobot must navigate to the desired location and be rotated to a given heading to punch successfully the considered tissue. To realize targeted drug delivery, the microrobot must also navigate to a specific region to control the drug release kinetics and modulate the concentration at the therapeutic window. To do so, the overall motion of the magnetic microrobot in the 3D workspace of the eyeball is simply summarized as its 3 translations and 2 rotations, that is with 5 degrees of freedom (DOF). The motion of microrobot can be controlled by either the applied magnetic field or its gradient. Basically, the magnetic field produces a magnetic torque  $\mathbf{t}_m$  in order to rotate the microrobot, perform a corkscrew swim, or a drilling operation. The magnetic gradient is commonly used to generate a pulling force  $\mathbf{f}_m$  to propel the microrobot or to perform a robotic task (e.g. puncture, peeling, etc.).

Finally, as shown in Figure 2, the external EMA platform should be conveniently placed in front of the head with a suitable distance with respect to the eye. Especially, the

<sup>2</sup> Collagen is the main structural protein in the extracellular matrix in the various connective tissues in the body.

<sup>3</sup> Hyaluronic acid (HA) is an anionic glycosaminoglycan (an amino sugar) that is a major component of synovial tissues and fluid.

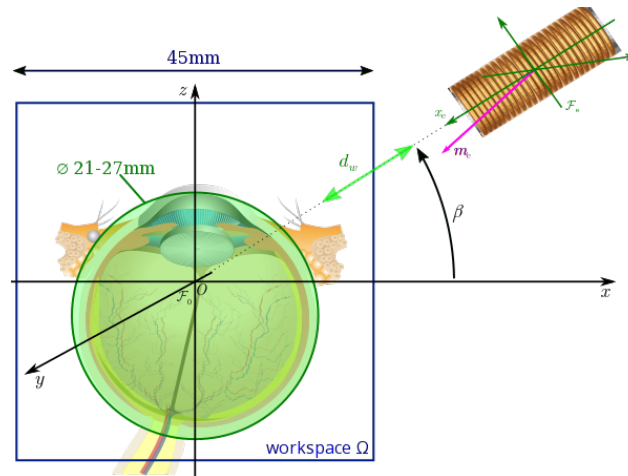


**Figure 3.** Representation of the workspace with respect to the eye geometry.

control of the magnetic actuation should precisely and reliably meet the requirements of the ophthalmic MIS procedure. The next section sets out the specifications for the design of such EMA platform regarding ophthalmic MIS operation.

### 2.2. Intraocular MIS operations requirements

First, the geometric constraints of the eyeball and the head should be considered. As reported by Bekerman *et al.* [27], the size of a human adult eye is about 22 mm to 27 mm, without significant difference between gender and age groups. Hence, the diameter of the considered workspace should be at least 27 mm. However, some extra spaces should be reserved for other eye tissues and the movement of eyeballs. Similarly, the workspace  $\Omega$  should be defined in respect of the working distance  $d_w$  between the workspace center  $O$  and the electromagnet, as reported in Figure 3. From the analysis carried in [2],  $d_w$  should be sufficiently small to enable strong magnetic field in  $\Omega$ . Based on these results and requirements, the workspace is defined as a cube of volume of  $\Omega = 45 \text{ mm} \times 45 \text{ mm} \times 45 \text{ mm}$  with a working distance  $d_w = 65 \text{ mm}$ .

In the considered intraocular application, the microrobot will evolve in the VH to perform the biomedical tasks. Basically, the VH is a complex transparent biofluid that exhibits non-Newtonian rheological properties. Commonly, two different phases is distinguished in VH: i) a liquid phase near the center of the eyeball, and ii) a gelatinous phase near the edges due to the presence of the network of collagen fibrils and hyaluronic acid [23–25]. Specifically, Bonfiglio *et al.* [23,24] report that the kinematic viscosity can be considered from  $5 \times 10^{-6} \text{ m}^2 \text{ s}^{-1}$  to  $8 \times 10^{-4} \text{ m}^2 \text{ s}^{-1}$ . While the density is in the range of  $1.0053 \text{ g m}^{-3}$  to  $1.0089 \text{ g m}^{-3}$ . VH liquid phase has a surface tension of  $47.8 \text{ mN m}^{-1}$ , that behaves like a typical viscoelastic gel, presenting an elastic region and followed by a delayed elastic region [25]. Therefore, the physiological properties of the medium are changing significantly, and the EMA platform should adapt the magnetic field and gradient distribution accordingly.

As reported by Amblard *et al.* [28], a force between 0.1 pN to 1 pN is enough for moving a micro-object through a moderately dense actin filament network. If the microrobot is made of SPIO material with a magnetization of 50emu/g with an equivalent diameter of about  $L \sim 2 \mu\text{m}$ , at least a magnetic field magnitude of about  $\|\mathbf{B}\| = 200 \text{ mT}$  and a magnetic gradient strength of  $0.1 \text{ mT/m}$  are required. Let us recall, that the necessary field intensity decreases or increases following a cubic power of the characteristic length ( $L^3$ ) of the magnetic material of the microrobot. Also, for some operation, such as human retinal vessel puncture, stronger magnetic forces are required. For instance, Dogangil *et al.* [29] report some experimental results on the required magnetic force for puncture tasks with an upper bound around 10mN. Their results are in agreement with medical data given by Gupta *et al.* [5] where it is reported that most puncture forces during vitreoretinal surgery

should be below 12.5mN. Obviously, smaller and sharper microneedles tip will reduce the required puncture forces [30]. Therefore, for microrobot of size of few  $L \sim 100\text{mm}$ , the required magnetic field strength could be assumed to be at least about  $\|\mathbf{B}\| = 15\text{mT}$ , and the magnetic gradient strength at least on the order of  $100\text{mT/m}$ . To summarize, the required amount of magnetic fields and gradients may vary according to the different tasks that has to be achieved by the medical microrobot, such as navigating in different VH phase, and performing the specified ophthalmic interventions (e.g. peeling, punctures...).

Given these biomedical specifications, the designed EMA platform must provide both the magnetic fields and gradients necessary to produce efficient magnetic torque  $\mathbf{t}_m$  and force  $\mathbf{f}_m$ . The magnetic fields distribution are affected by many parameters, including the number of electromagnets or their arrangement, also by their shape and material properties. Secondly, to allow a reliable and efficient ophthalmic MIS intervention, the characteristic of these fields must be able to adapt the task in progress. Thereby, the reconfigurable EMA setup fulfilling the application objectives will be designed in detail in the following section using the methodology described in [3].

### 3. OctoRob Platform Design

The effective design of the EMA setup must best meet the requirements for the considered application objectives set out in the previous section. Since the main components of the system are the electromagnetic coils, it is necessary to determine their number, arrangement, material properties, geometry and size.

From the previous investigation [2,31], at least either  $n = 8$  stationary electromagnets or  $n = 5$  mobile electromagnets sources are required to perform 3D magnetic manipulation in the eyeball. As mentioned in [3], with more coils the EMA setup are able to provide more strong, flexible and less-singular magnetic control. Therefore, we have chosen to use  $n = 8$  electromagnets to design the OctoRob platform.

Next, with the suitable electromagnets set, the first issue is to choose the configuration arrangement of the electromagnets around the human head. Indeed, the chosen configuration must yield the human head geometry allowing the eyeball as workspace (see Figures 2 and 3). Commonly, the minimum size of the workspace is restricted by the dimension of the coils, which is also related to the shortest distance  $d_w$ . Obviously, the larger electromagnetic coil leads to a more powerful magnetic source, but it will make the coils more crowded surrounding the workspace. Furthermore, the larger coils generally require longer distance  $d_w$ . Thus, the maximum diameter of electromagnets can be obtained through their most compact geometric arrangement considering a working distance with a value of  $d_w = 65\text{mm}$ .

From the previous studies, either the OctoMag-like or the MiniMag-like configuration seems to be a proper arrangement solution to fulfill the OctoRob design specifications. Besides, the realized OctoRob system should be adaptable and adjustable in real-time with respect to the microrobotic task. The distance ( $d_w$ ) and orientation ( $\beta$ ) of each electromagnet are the most important parameters to be adjusted [3]. Specifically, the adaptation of the moving angle  $\beta$  of a mobile coil set makes it possible to favor either the magnetic field or its gradient. That is why a kinematic mechanism should be devised in order to adapt in real-time the orientation of each movable electromagnet.

The reconfigurable electromagnet system is realized by the use of robotic arms. Since the mobile angle  $\beta$  at the end-effector of the robotic arm is the sole parameter, only the kinematic rotation is utilized to achieve dynamic analysis. Thereby, the simulations of the realized robotic EMA system will be further investigated for the estimation of its performance. These different aspects are presented in the following sections.

#### 3.1. Modeling of multipole electromagnetic coils system

3 magnetic fields and 5 magnetic gradients inputs are required to achieve up to 5 DOFs control of microrobot without singularity [2,32]. Let us consider an overall magnetic field  $\mathcal{F}_0 \mathbf{B}(\mathbf{p})$  generated by a set of  $n$  electromagnets at any point  $\mathbf{p}$  within the workspace  $\Omega$ , as

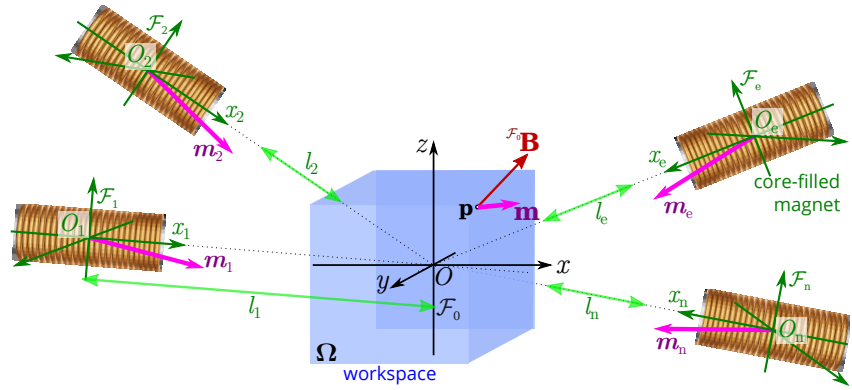


**Figure 4.** Representation of the multipole electromagnets system to induce a magnetic field  $\mathbf{B}(\mathbf{p})$  in the workspace  $\Omega$  (blue square box). The length  $l_e$  denotes the distance between the coil center  $O_e$  to the workspace center  $O$ .

presented in Figure 4. This global magnetic field is basically the sum of the contributions of all individual electromagnets  $e$ .

To evaluate the magnetic field  $\mathbf{B}_e(\mathbf{p})$  induced by the electromagnets  $e$ , models based either on numerical or analytical approaches are commonly considered. Numerical methods are generally based on the interpolation of the magnetic field obtained either from finite element method (FEM) or from an experimental measurement of the field  $\mathbf{B}_e$  [4]. Such numerical methods provide high-precision magnetic field calculations, but they are very time-consuming. To speed up the computations, analytical methods commonly based on dipole approximation or even on elliptical integrals are used [4,33–35]. Hybrid approaches, using a map of the magnetic field obtained from FEM and a fitting of an analytical model can be also considered [4]. The choice of method usually results in the best balance between speed and accuracy. Here, we assume that the magnetic field  $\mathbf{B}_e(\mathbf{p})$  of each point  $\mathbf{p}$  in  $\Omega$  is approximated by the magnetic point-dipole model. In the workspace as shown in Figure 4, the point-dipole model indicating the magnetic field  ${}^{\mathcal{F}_e}\mathbf{B}_e$  of the coils  $e$  wrt. its own frame  $\mathcal{F}_e(O_e : x_e, y_e, z_e)$  is expressed as:

$${}^{\mathcal{F}_e}\mathbf{B}_e(\mathbf{p}) = \frac{\mu_0}{4\pi|\mathbf{p}|^3} \left( \frac{3(\mathbf{m}_e \cdot \mathbf{p})}{|\mathbf{p}|^2} \mathbf{p} - \mathbf{m}_e \right) \quad (1)$$

with  $\mathbf{m}_e$  the equivalent magnetic dipole moment of the electromagnetic coil  $e$  for a unit current input ( $i_e = 1$ ).

The magnetic field  ${}^{\mathcal{F}_e}\mathbf{B}_e(\mathbf{p})$  should be expressed in the reference frame  $\mathcal{F}_0(O : x, y, z)$  by the homogeneous transformation:

$${}^{\mathcal{F}_0}\mathbf{B}_e(\mathbf{p}) = {}^{\mathcal{F}_0}\mathbf{T}_{\mathcal{F}_e} \times {}^{\mathcal{F}_e}\mathbf{B}_e(\mathbf{p}) \quad (2)$$

where the homogeneous transformation matrix is basically defined as:

$${}^{\mathcal{F}_0}\mathbf{T}_{\mathcal{F}_e} = \left( \begin{array}{c|c} {}^{\mathcal{F}_0}\mathbf{R}_{\mathcal{F}_e} & {}^{\mathcal{F}_0}\mathbf{t}_{\mathcal{F}_e} \\ \hline \mathbf{0} & 1 \end{array} \right)$$

where  ${}^{\mathcal{F}_0}\mathbf{R}_{\mathcal{F}_e}$  is the rotation matrix and  ${}^{\mathcal{F}_0}\mathbf{t}_{\mathcal{F}_e}$  represents the translation matrix regarding the reference frame  $\mathcal{F}_0$ . Therefore, the global magnetic field distribution in the workspace generated by a set of  $n$  electromagnetic coils can be superimposed as:

$${}^{\mathcal{F}_0}\mathbf{B}(\mathbf{p}) = \sum_{e=1}^n {}^{\mathcal{F}_0}\mathbf{B}_e(\mathbf{p}) = ({}^{\mathcal{F}_0}\tilde{\mathbf{B}}_1(\mathbf{p}) \quad \dots \quad {}^{\mathcal{F}_0}\tilde{\mathbf{B}}_n(\mathbf{p})) \mathbf{i} = {}^{\mathcal{F}_0}\mathcal{B}(\mathbf{p}) \mathbf{i} \quad (3)$$

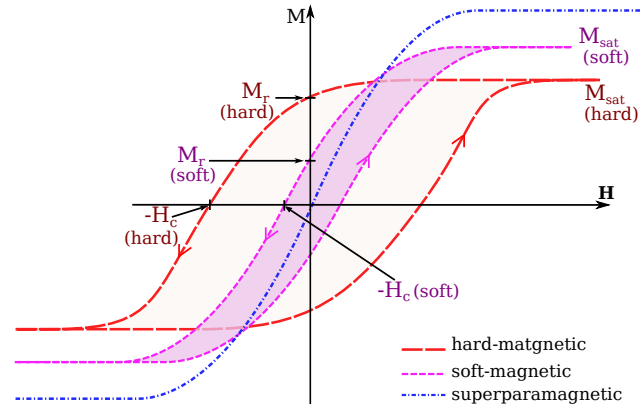


**Figure 5.** Typical hysteresis curve for ferromagnetic materials. The intercepts  $H_c$  and  $M_r$  are the intrinsic coercivity and magnetization remanence.

with  $\mathbf{i} = (i_1, i_2, \dots, i_n)^\top$  the applied electrical currents. This relation (3) shows that the induced magnetic field  ${}_{\mathcal{F}_0}\mathbf{B}(\mathbf{p}, \mathbf{i})$  and its gradient in the workspace can be adjusted by controlling the flowing currents  $\mathbf{i}$ . When the electromagnet is dynamically moved, either the magnetic field or the gradient can be favored.

### 3.2. Electromagnetic coil design

The core-filled electromagnet has been selected to OctoRob system. The core-filled electromagnet is able to generate a stronger magnetic field than the air-filled electromagnet since the magnetic core can concentrate the magnetic field. Basically, the magnetic material, the shape, the geometry of the core are the key design parameters of the electromagnet.

#### 3.2.1. Magnetic core

The presence of a magnetic core involves some non-linearity and coupling between the electromagnets in the magnetic field distribution. Furthermore, different loss effects occur when the flowing current is varying in the coils, such as winding, eddy currents and hysteresis losses. Therefore, the choice of its material is an important issue. Basically, soft-ferromagnetic material should be favored [36]. Indeed, to select an efficient magnetic core material, its permeability, saturation magnetization ( $M_{sat}$ , A/m) and coercivity ( $H_c$ , A/m) are the main relevant characteristics, as illustrated in Figure 5. The higher permeability and saturation magnetization are preferred for flux confinement and focusing. Whereas, a low coercivity is important for high-frequency applications and to reduce the core losses. Table 1 reports properties of some common soft-magnetic materials. Moreover, some additional constraints should be also considered in the choice of the core material. For instance, to deal with mechatronic constraints, its weight may come an essential issue. Obviously, the cost of the material is also a significant factor in the final choice.

The shape of its tip should then be determined. Commonly, flat-faced, rounded and sharp-faced magnetic cores have been investigated by researchers [39,40]. In particular, if the tip of the magnetic core is not flat but pointed or round, the magnetic field is nonuniform and severely distorted. In contrast, the use of sharp-faced allows the generation of higher magnetic field and a larger field gradient near the electromagnet. For instance, the effect of core tip geometry on magnetic field projection is evaluated and reported by Kummer [39] with the FEM analysis. The analysis appears that the more soft-magnetic material is packed up to the very edge of the coil, the more induced magnetic field will be emitted, and electromagnet will generate a stronger magnetic field. For our application objective with a working distance of  $d_w = 65\text{mm}$ , flat-faced tip (or equivalent cylindrical tip) can make electromagnet to generate the strongest and the most uniform magnetic field in a workspace of  $\Omega = 45\text{mm} \times 45\text{mm} \times 45\text{mm}$ . However, the flat-faced tip could cause more crowded space when the  $n = 8$  electromagnetic coils are arranged together around the workspace. Especially, it is clear that the induced magnetic field will be enhanced when

**Table 1.** Typical properties of some soft-magnetic materials. (adapted from [37–39])

Material	Saturation (A/m)	Remanence (T)	Coercivity (A/m)	Relative permeability ( $\mu_r$ )	Density (kg/m <sup>3</sup> )
Cobalt (Co)	$2.4 \times 10^6$	0.5	795.7	250	890
Iron (Fe)	$3.1 \times 10^6$	1.3	79.5	5000	7874
Nickel (Ni)	$5.1 \times 10^5$	0.4	55.7	600	8908
Low carbon steel <sup>a</sup>	$1.7 \times 10^6$	0.9	397	1560	7850
FeCo alloy <sup>b</sup>	$1.8 \times 10^6$	1.6	100	7000	8120
FeNi alloy <sup>c</sup>	$1.2 \times 10^6$	1.1	2.8	190000	8200

<sup>a</sup>properties for C35 standard carbon steel with 0.35% C, 0.15% Si, 0.5% Mn, and 0.015% S

<sup>b</sup>properties for Vacoflux<sup>®</sup>50, from Vacuumschmelze GmbH, that is composed of 49% Fe, 49% Co, 2% V

<sup>c</sup>properties for Supra50, from Aperam S.A., a Mu-metal that is composed of 51.9% Fe, 47.5% Ni, 0.5% Mn, 0.1% Si

magnetic core increases its volume. Thereby, with sufficient space for the electromagnet to move, the core-filled electromagnet can be enlarged to increase the induced magnetic field strength. The electromagnet dimensions will be discussed hereafter.

### 3.2.2. Optimal electromagnets sizing

Suitable electromagnet dimension is important for generating the necessary magnetic field and gradient in a limited workspace  $\Omega$ . The requirement for magnetic manipulation in the compatible intraocular procedure leads to a working distance of about  $d_w = 65\text{mm}$ . As mentioned in Figure 6, the different coils of the OctoRob platform are divided in two sets: i) four stationary electromagnets:  $e = i = 1..4$ ; and ii) four mobile coils:  $e = j = 5..8$ . These two sets are arranged around a common z-axis with an azimuth angle  $\alpha_e = 45^\circ$  ( $e = 1..8$ ), and are pointing to the common center  $O$ . We consider that the  $n = 8$  electromagnets are identical with a cylindrical geometry and an external radius<sup>4</sup>  $r$ . They are initially considered placed to get the maximum value  $r_{\max}$  of their dimension. Specifically, the largest  $r_{\max}$  is obtained when all coils are closely contacted with their neighboring. In our case, any mobile coils are in contact with all its adjacent coils (either a mobile or stationary ones). However, the stationary coil set is in contact only with the neighboring mobile coils, but not with the other (stationary) coils. For instance, the stationary coil  $i = 1$  touches the  $j_1 = 5$  and  $j_2 = 8$  ones; whereas the mobile coil 5 is in contact with 2, 6, 1 and 8.

Figure 6 represents the geometric view of the  $n = 8$  electromagnetic coils, where the cyan lines denote the distance  $d_w = OO_e$  from the tip center  $O_e$  of the electromagnet  $e$  to the workspace center  $O$ ; the yellow lines represent its external radius  $r$ ; and the green lines indicate the distance between the core center  $O_e$  to the adjacent contacting electromagnets. First, due to the axisymmetric arrangement, the distance  $d_{i_1i_2} = O_{i_1}O_{i_2}$  between two neighboring stationary coils  $i_1$  and  $i_2$  are identical; in the same way, all distances  $d_{j_1j_2} = O_{j_1}O_{j_2}$  between two adjacent moving coils  $j_1$  and  $j_2$  are equal. Next, each electromagnet has a cylindrical face of radius  $r$ . It can be shown that  $r$  is tangent to the sphere of radius  $d_w$ , and they are on a same plane for the two contacting coils, and then  $OO_e = d_w$  and  $r$  intersect at right angles ( $90^\circ$ ), as represented in Figures 6(b)-(c) and 7. As all coils share the same radius  $r$  and working distance  $d_w$ , for stationary coils  $i = 1..4$  and their adjacent mobile coils  $j = 5..8$ , the distances<sup>5</sup>  $d_{ij} = O_iO_j$  all have the same length. Thus, a mobile coil  $j = 5..8$  and its two adjacent stationary coils  $i_1$  and  $i_2$  form an isosceles triangle  $O_{i_1}O_jO_{i_2}$ , and in the same way  $O_{j_1}O_iO_{j_2}$  also form an isosceles triangle. Following the same

<sup>4</sup> The external radius encompass the core, the coil winding, and eventually the cooling part.

<sup>5</sup>  $O_iO_j$ : possible cases are  $O_1O_5, O_2O_5, O_2O_6, O_3O_6, O_3O_7, O_4O_7, O_4O_8$ , and  $O_1O_8$ .

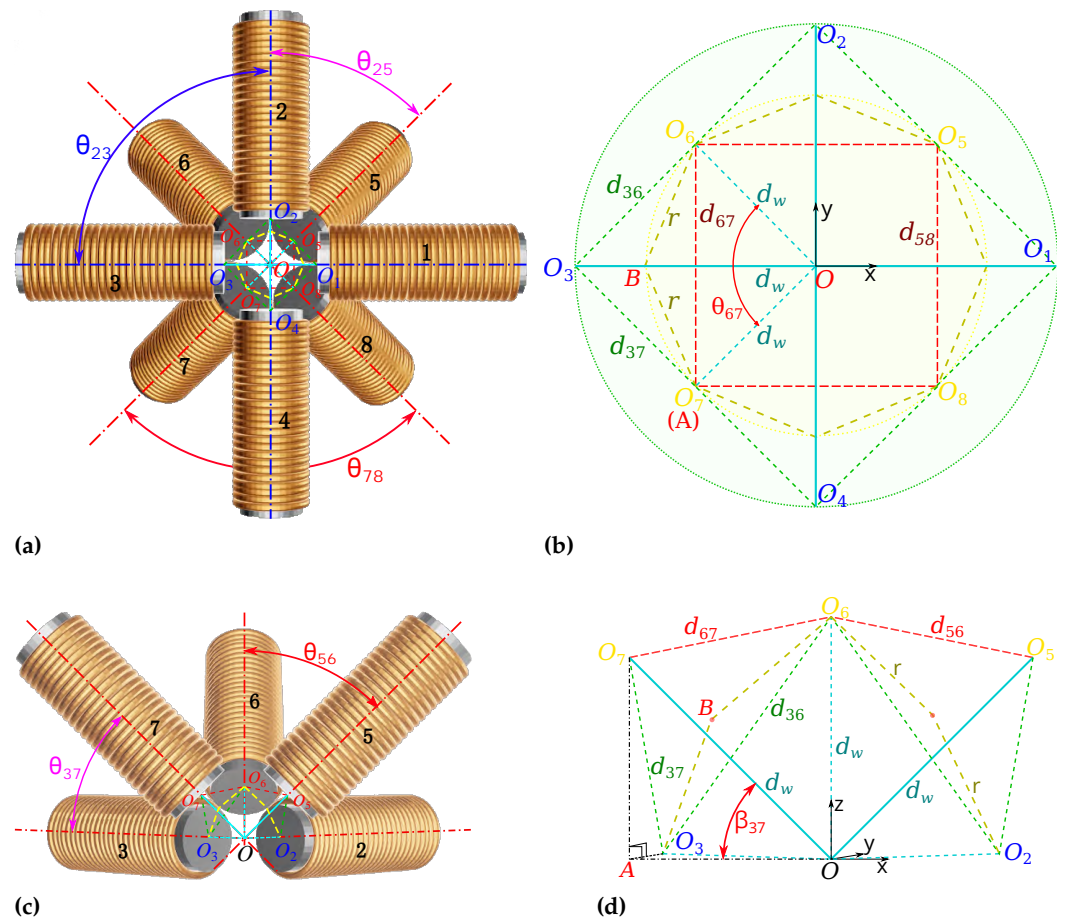


**Figure 6.** Representation of the geometric arrangement of the 3D  $n = 8$  electromagnetic coils: (a) top views; (c) side views where three electromagnetic coils are removed to show clearly internal space; (b) and (d) show the geometry between the electromagnets center  $O_e$ . The plain lines depict the in-plane lengths, whereas dashed lines represent the out-of-plane one.

reasoning, it can be seen that all angles<sup>6</sup>  $\theta_{j_1j_2}$  between two adjacent mobile coils  $j_1$  and  $j_2$  are identical; and similarly, every angle<sup>7</sup>  $\theta_{ij}$  between a mobile coil  $j$  and a neighboring stationary coil  $i$  has the same value, respectively.

To determine the maximum value  $r_{\max}$  for every angle  $\beta_i$  and  $\beta_j$ , let us define the projection  $P_e$  of the center  $O_e$  of the electromagnet  $e$  in the  $xy$ -plane, as represented in Figure 7a. As one can see, each angle  $\theta_{ij}$  is defined as:

$$\theta_{ij} = 2 \arcsin \left( \frac{d_{ij}}{2d_w} \right)$$

<sup>6</sup>  $\theta_{j_1j_2}$ : possible cases are  $\theta_{56}$ ,  $\theta_{67}$ ,  $\theta_{78}$  and  $\theta_{85}$ .

<sup>7</sup>  $\theta_{ij}$ : possible cases are  $\theta_{15}$ ,  $\theta_{25}$ ,  $\theta_{26}$ ,  $\theta_{36}$ ,  $\theta_{37}$ ,  $\theta_{47}$ ,  $\theta_{48}$  and  $\theta_{18}$ .

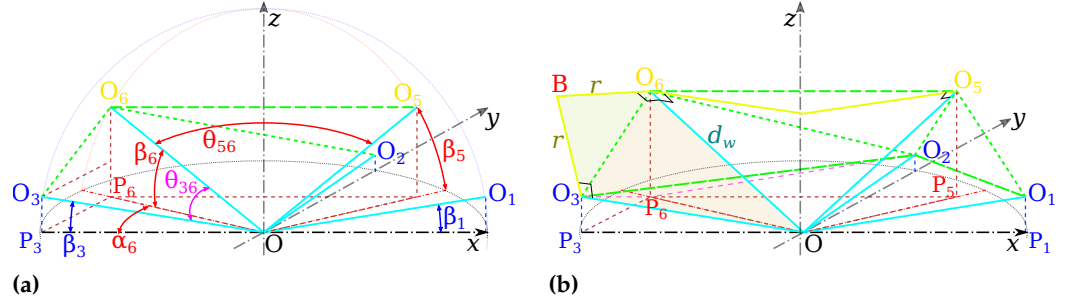


**Figure 7.** Representation of (a) the angles and (b) lengths definitions.

with the length  $d_{ij} = O_i O_j = \sqrt{P_i P_j^2 + (O_j P_j - O_i P_i)^2}$ , where

$$\begin{aligned}
 P_i P_j &= \sqrt{OP_i^2 + OP_j^2 - 2(OP_i)(OP_j) \cos \alpha_j} \quad (\text{here } \alpha_j = 45^\circ) \\
 O_i P_i &= d_w \sin \beta_i \\
 O_j P_j &= d_w \sin \beta_j \\
 OP_i &= d_w \cos \beta_i \\
 OP_j &= d_w \cos \beta_j
 \end{aligned} \tag{4}$$

Similarly, the angle between two adjacent mobile coils  $j_1$  and  $j_2$  is derived as:

$$\theta_{j_1 j_2} = 2 \arcsin \left( \frac{d_{j_1 j_2}}{2d_w} \right)$$

where  $d_{j_1 j_2} = O_{j_1} O_{j_2} = \sqrt{OP_{j_1}^2 + OP_{j_2}^2}$ . If all mobile coils  $j$  have the same moving angle  $\beta_j$ , then we obtain:  $d_{j_1 j_2} = \sqrt{2}d_w \cos \beta_j$  from (4). When a stationary coil  $i$  touches a mobile coil  $j$ , their radii must be:

$$r_{ij} = \frac{d_{ij}}{2 \cos(\theta_{ij}/2)} = \frac{d_{ij}}{2 \sqrt{1 - \left(\frac{d_{ij}}{2d_w}\right)^2}}$$

and when a mobile coil  $j_1$  is in contact with a mobile coil  $j_2$ , their radii are defined as:

$$r_{j_1 j_2} = \frac{d_{j_1 j_2}}{2 \cos(\theta_{j_1 j_2}/2)} = \frac{d_{j_1 j_2}}{2 \sqrt{1 - \left(\frac{d_{j_1 j_2}}{2d_w}\right)^2}} \tag{5}$$

Since all radii are equal, we get:  $r_{max} = r_{ij} = r_{j_1 j_2}$ . Hence, it can be shown that the maximal admissible radii are obtained when

$$2 - \sqrt{2} \cos(\beta_i) \cos(\beta_j) - 2 \sin(\beta_i) \sin(\beta_j) = 2 \cos(\beta_j)^2$$

Figure 8 shows the evolution of the admissible radius  $r_{max}$  and of mobile angle  $\beta_j$  when the contact constraints are satisfied. For instance, when the OctoMag configuration is considered [4],  $\beta_i = 0$  for the stationary coil set leads to  $\beta_j = 45^\circ$  for the moving coil set (or the upper set equivalently). Obviously,  $d_{ij} = d_{j_1 j_2} = d_w$  can be computed from the above equations that brings the maximum coil dimension. Thus, when the  $d_w$  is set to 65mm, the radius of  $r_{max} = 37.5278\text{mm}$  can be derived.

### 3.2.3. Coil implementation

As specified, a cylindrical electromagnetic coil is considered in this platform, as depicted in Figure 9. In such case, the magnetic performance can be approximated using

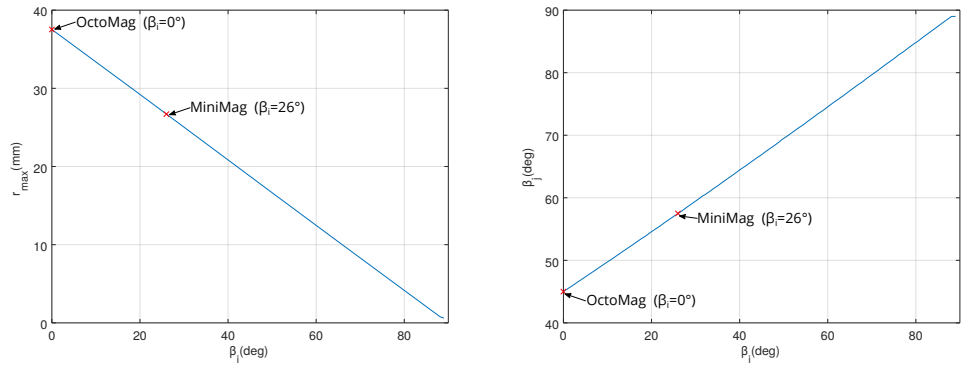


**Figure 8.** Evolution of (a) admissible radius  $r_{max}$  and (b) the mobile angle  $\beta_j$  when the contact constraints are satisfied.

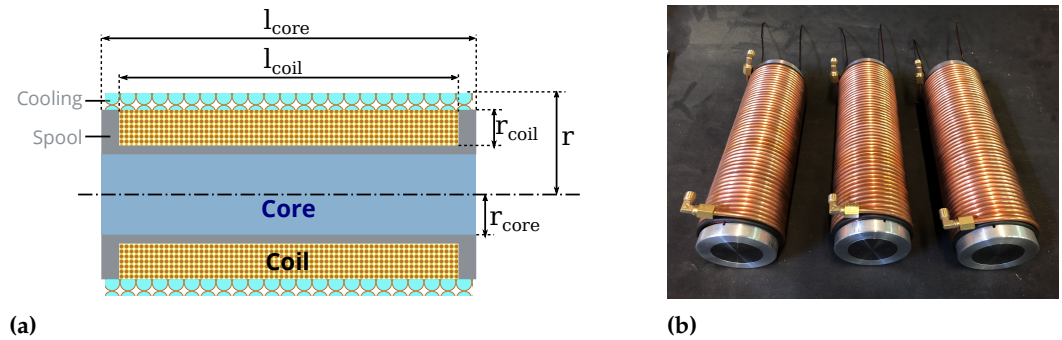


**Figure 9.** (a) illustrates the electromagnet shape, with its core, coil winding and its cooling part. The spool part allows containing the winding and to separate it from the core. (b) presents the implemented electromagnet prototype.

a solenoid model. Indeed, the magnetic field strength at the end of an infinite solenoid corresponding to an electromagnet  $e$  is given by [41] through applying the Ampère's law:

$$\|B_e\| = \mu \frac{i_e N}{2l} \quad (6)$$

with  $i_e$  the electric current,  $l$  the length of the solenoid, and  $N$  the number of turns of the coil winding.

To maximize the magnetic field strength, two parts of the electromagnet can be optimized: i) the core and its permeability performance  $\mu$ ; and ii) the coil winding. To do so, when the maximum allowable electromagnet size  $r_{max}$  with respect to the spatial arrangement is determined, its remaining dimensions could be estimated easily. Kummer [39] has proposed an electromagnet design that takes into consideration further constraints. Specifically, they have shown that the proper length to radius ratio of the core should be at least  $l_{core}/r_{core} \geq 8$  to fit properly the above solenoid characteristics. From their results, it appears that a core with a radius of about  $r_{core} \approx 20\text{mm}$  and then a length  $l_{core} = 10 \times r_{core}$  enable reliable magnetic field performance.

Next, the coil thickness should be determined. From the infinite solenoid (6), the best magnetic performance is achieved when the number of turns  $N$  is maximized. However, the winding of coil is limited by the current density that would cause safety issue. Basically, from transformer design, without cooling, it is shown that the current density should not exceed  $J_{max} = 3\text{A}/\text{mm}^2$ . Nevertheless, to enable strong magnetic field, the current  $i_e$  must be high enough. Therefore, the parameter of  $J_{max} = 3\text{A}/\text{mm}^2$  normally requires

the wire made of a larger cross-section of conductor that will limit the number of turns  $N$ . In order to increase  $i_e$  together with a great  $N$  in a limited room, a cooling system will be mandatory. Different strategies can be envisioned for the cooling part, such as using fan, radiator vent, or water/coolant system. Classically, using a circulating coolant is the most effective technology to cool a system.

From these considerations, we have chosen the following design parameters to implement each electromagnet. The core is composed of low carbon steel (C35, ThyssenKrupp AG, France) with  $r_{core} = 21\text{mm}$  and  $l_{core} = 240\text{mm}$ . An aluminum<sup>8</sup> (Aluminum EN AW-2017a-en 573-3, ThyssenKrupp AG, France) spool is added to separate the core and the coil, and to keep the winding in the given space. This spool has an inner length of  $l_{coil} = 210\text{mm}$  and a thickness of 1mm. The coil is composed of winding of 6 layers of copper<sup>9</sup> wire (Enameled copper wire, cl 200 degrees, grade 2. APX, France) of diameter of 1.6mm, leading to a thickness of 9.6mm and a number of turns  $N = 787$ . Finally, a cooling unit is placed around the coil winding. The cooling system consists of a circulating coolant liquid flowing through a copper tube with a diameter of 4mm. All these elements lead to an electromagnet with an overall size of  $r = 35.6\text{mm}$ , and electromagnet prototype has been realized and is shown in Figure 9b.

### 3.2.4. Coil performance evaluation

The methodology used in the simulation is based on the assumption that the point-dipole model (1) approximates properly the magnetic field distribution. The assumption is validated in this section.

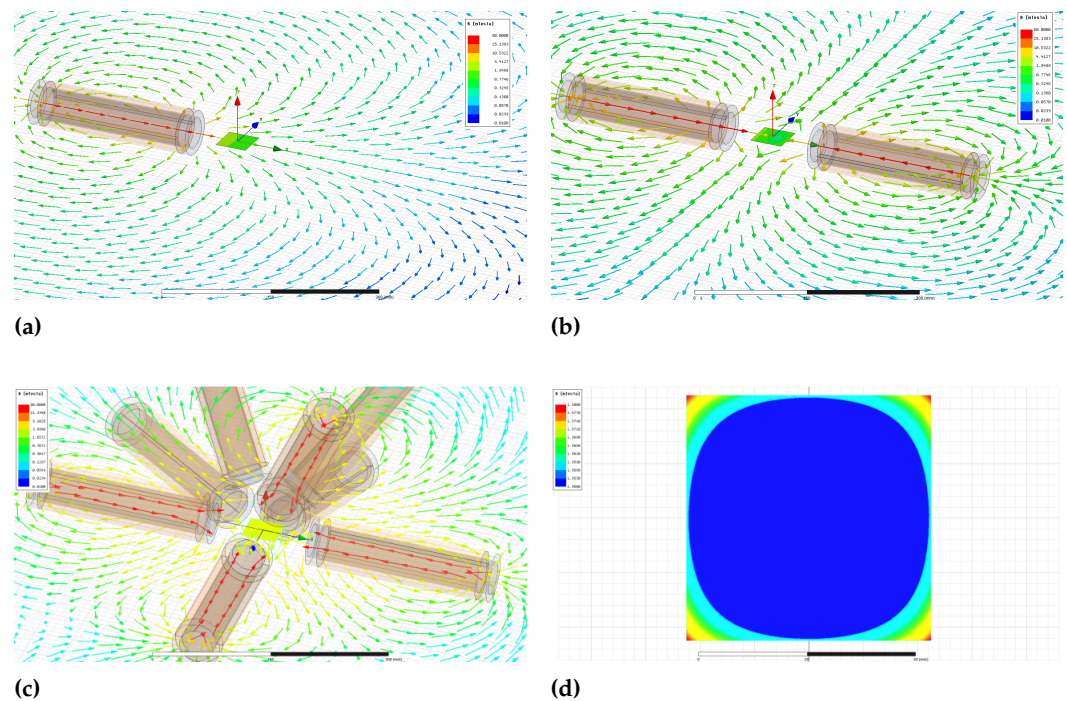


**Figure 10.** Magnetic field distribution using FEM: (a) a single and (b) a dual electromagnets systems; and (c)-(d) the  $n = 8$  electromagnets arrangement with  $\beta_i = 0^\circ$  and  $\beta_j = 45^\circ$ . (d) shows the magnetic field magnitude within the workspace.

FEM modeling using ANSYS<sup>®</sup> Maxwell<sup>10</sup> software has been performed. Hence, the specified electromagnetic coils have been modeled and simulated through finite element

<sup>8</sup> Aluminum is a paramagnetic material that is essentially unaffected by the magnetic fields.

<sup>9</sup> Copper is a diamagnetic material, and thus is repelled by the magnetic field.

<sup>10</sup> <https://www.ansys.com/products/electronics/ansys-maxwell>

analysis (FEA). Figure 10 shows some simulation results where a current of  $1\text{A/turn}$  is flowing in each electromagnet. Figures 10(a)-(b) illustrate the magnetic field  $\mathbf{B}$  where the workspace is surrounded by a single and a pair of electromagnet(s), respectively. Likewise, Figures 10(c)-(d) present the magnetic field distribution of the retained  $n = 8$  electromagnets' configuration where the stationary coil set has an angle  $\beta_i = 0$  and the mobile coil set has an angle  $\beta_j = 45^\circ$ . Figure 11 shows the comparison between the FEM results and the point-dipole results along the  $x$ -axis. Especially, Figure 11b reports the relative error on the magnetic field magnitude within the workspace. It appears that the point-dipole model is a convenient method to approximate the magnetic field distribution with a relative error less than  $|3.5|\%$  in the OctoRob workspace.

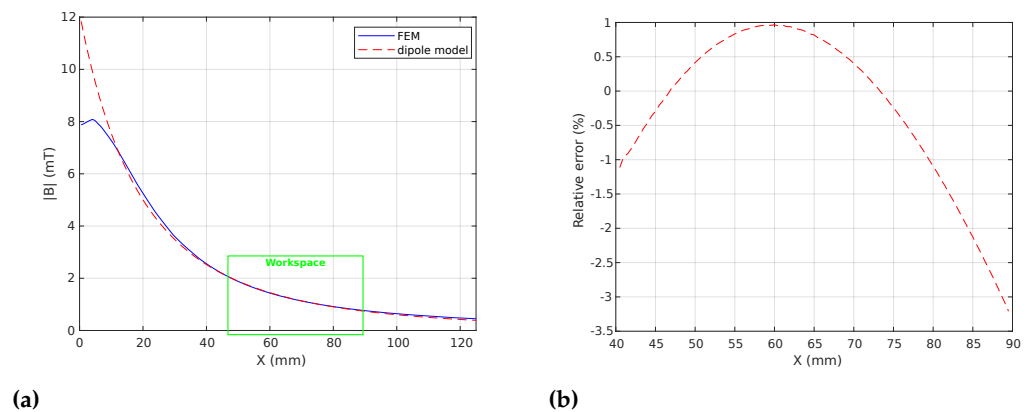


**Figure 11.** Comparison simulation results between FEM and point-dipole model along the  $x$ -axis: (a) the magnetic field magnitude where the green box delimit the range of workspace, and (b) the relative error within the workspace.

### 3.3. Design of the robotic arm

The previous motivations and application specifications lead to making the OctoRob platform reconfigurable. This makes it possible to favor sometimes the magnetic field and the torque, sometimes the magnetic field gradient and the traction/thrust force. To achieve this, we propose the design of a robotic arm mechanism for controlling electromagnet orientation in the following.

#### 3.3.1. Robotic arm mechanism description

The OctoRob platform must be able to move the mobile coils independently, i.e. their polar angles  $\beta_j$  should be changed dynamically. A basic solution for actuating the robotic arm is to use simple DC motors. However, its placement must be studied to limit magnetic field interference and prevent electromagnetic compatibility (EMC) issue. To overcome this problem, the moving coils are placed at the end-effector of a robotic arm, as illustrated in Figure 12. Based on these considerations, and as only 1 DOF is required, we have chosen to use a well known four-bar linkage mechanism. Especially, the four-bar linkage architecture allows reliable 1 DOF motion feature, higher energy efficiency, good rigidity, less link inertia and compact drive systems.

Figure 12b depicts the kinematic chain of the designed four-bar linkage. Specifically,  $L_1$  is the crank,  $L_2$  the coupler and  $L_3$  the rocker. In addition, the frame  $L_4$  is decomposed in four parts:  $L_{4a}$ ,  $L_{4b}$ ,  $L_{4c}$  and  $L_{4g}$ . Each link or part  $L_i$  has a length  $r_i$ . In particular, the lengths  $DE = r_2$ , and  $CH' = r_{3a}$  can be easily adjusted manually to modify the kinematics of the electromagnet. The lengths  $GA = r_{4a}$  and  $AB = r_{4b}$  could be also modified to handle smaller or bigger electromagnetic coils if it is necessary. Once fixed and calibrated, the links' geometry of the OctoRob platform cannot vary, and would lead to the simplified kinematics chain shown in Figure 12c. Table 2 presents some calibrated parameters of the

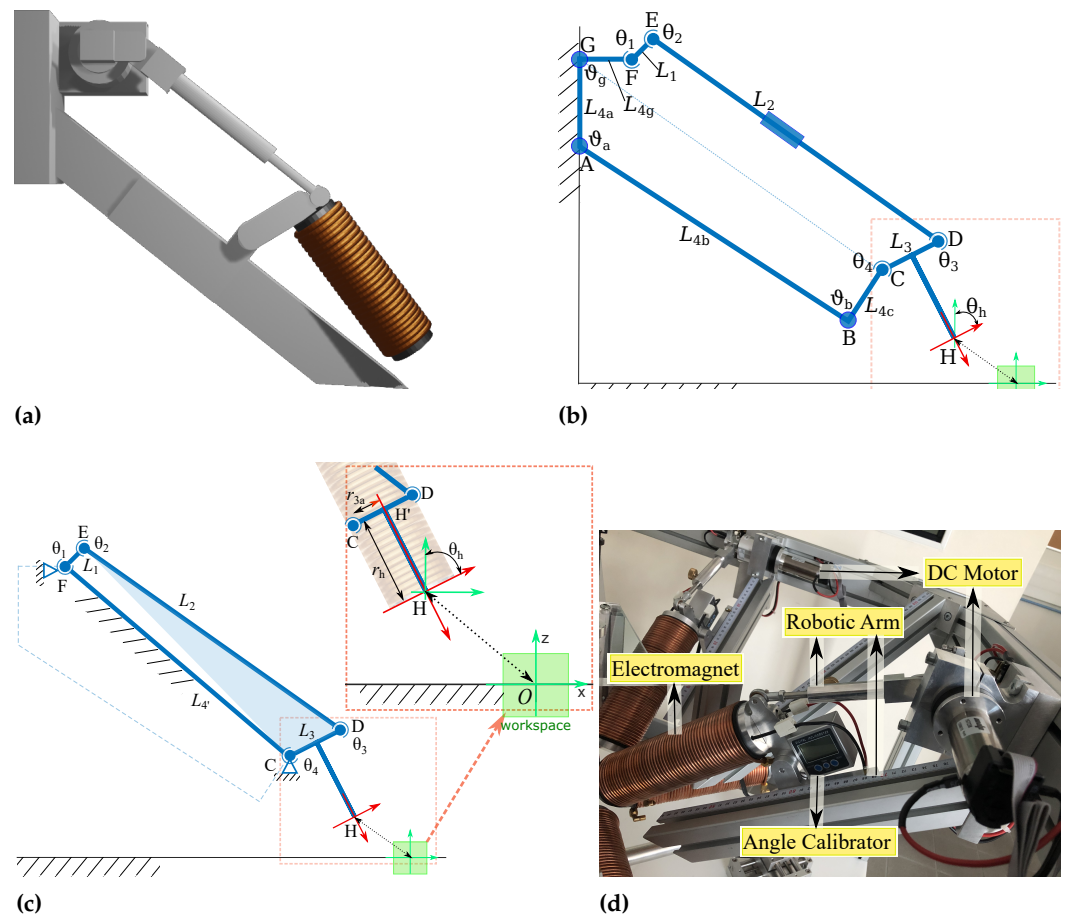


**Figure 12.** Representation of the robotic arm: (a) CAD illustration of the concept, (b)-(c) show the kinematics chain with the four links  $L_1$ - $L_4$  and joints  $\theta_1$ - $\theta_4$ , and (d) represents the realized 1-DOF robotic arm.

robotic arm. With the proposed specifications, the robotic arms are realized and installed with electromagnets, DC motors, and angle calibrators, as represented in Figure 12d

**Table 2.** Parameters of the robotic arm<sup>†</sup>: (a) the simplified four-bar mechanism as in (c); and (b) the detail of the components of the link  $L_4$ .

(a)					(b)				
Link	$L_1$	$L_2$	$L_3$	$L_4$	Part	$L_{4a}$	$L_{4b}$	$L_{4c}$	$L_{4g}$
$r_i$ (mm)	33	444	75	372	$r_i$ (mm)	100	365	68	60
$\theta_i$	$\theta_1$	$\theta_2$	$\theta_3$	$\theta_3$	$\theta_i$	$123^\circ$	$90^\circ$	-	$90^\circ$

<sup>†</sup>The robotic arm is made of aluminum material.

Next, a motor actuates the joint  $\theta_1$ , that rotates the following links  $L_2$ - $L_3$  and the other joints  $\theta_2$ - $\theta_4$ . Then, the electromagnet fixed to the link  $L_3$  is able to rotate with  $\theta_h$ .

### 3.3.2. Kinematic analysis

As mentioned in Section 3.1, the magnetic field  $\mathcal{F}_0 \mathbf{B}(\mathbf{p})$  can be expressed in the reference frame  $\mathcal{F}_0$  linked to the workspace center by using the homogeneous transformation as in Equation (2). Similarly, the input angle  $\theta_1$  is transferred to the output angle  $\theta_h$  through applying transformation matrices. For more details of analysis of its definition of transformation, please see Appendix A.

The position of the point  $G$  is fixed, and we assume that its location is known with respect to the reference frame  $\mathcal{F}_0$  as  ${}^{\mathcal{F}_0}G = (x_g, y_g, z_g, 1)^\top$  in homogeneous coordinates. Next, when  $L_{4a} - L_{4c}$  are set to a given value, the position  $C = (x_c, y_c, z_c, 1)^\top$  of the joint  $\theta_4$  is fixed and can be determined in  $\mathcal{F}_0$  as:

$${}^{\mathcal{F}_0}C = \text{Rot}_y(\vartheta_b)\text{Trans}_z(r_{4c})\text{Trans}_x(r_{4b})\text{Trans}_z(-r_{4a}) {}^{\mathcal{F}_0}G$$

where  $\text{Rot}_y(\vartheta_b)$  denotes the pure rotation operation along the  $y$ -axis with angle  $\vartheta_b$ , and  $\text{Trans}_z(r_{4c})$  indicates a pure translation along the  $z$ -axis with the displacement  $r_{4c}$ .

Similarly, the location of  $E = (x_e, y_e, z_e, 1)^\top$  of the joint  $\theta_2$  can be expressed in  $\mathcal{F}_0$  as follows:

$${}^{\mathcal{F}_0}E = \text{Rot}_y(\theta_1)\text{Trans}_z(r_1)\text{Trans}_x(r_{4d}) {}^{\mathcal{F}_0}G$$

Through the transformation operations, the position of the end-effector  ${}^{\mathcal{F}_0}H$ , together with the point  ${}^{\mathcal{F}_0}H'$  can be determined by:

$$\begin{aligned} {}^{\mathcal{F}_0}H' &= \text{Rot}_y(\theta_3)\text{Rot}_y(\vartheta_b)\text{Trans}_z(r_3)\text{Trans}_z(r_{4c})\text{Trans}_x(r_{4b})\text{Trans}_z(-r_{4a}) {}^{\mathcal{F}_0}G \\ {}^{\mathcal{F}_0}H &= \text{Rot}_y(\pi/2)\text{Rot}_y(\theta_3)\text{Rot}_y(\vartheta_b)\text{Trans}_z(r_h)\text{Trans}_z(r_3)\text{Trans}_z(r_{4c})\text{Trans}_x(r_{4b}) \\ &\quad \times \text{Trans}_z(-r_{4a}) {}^{\mathcal{F}_0}G \end{aligned}$$

The orientation  $\theta_h$  of the end-effector can be then determined by the obtained  $\theta_3$  since the surface of electromagnet is parallel to  $L_3$ , that is:  $\theta_h = \theta_3$ . Therefore, both position and orientation parameters of the end-effector can be computed.

#### 4. Implementation of the OctoRob Prototype

From the design specifications, we fabricated the OctoRob platform illustrated in Figure 13. It is composed of four mobile robotic arms to control the mobile electromagnets orientation and four stationary electromagnets.

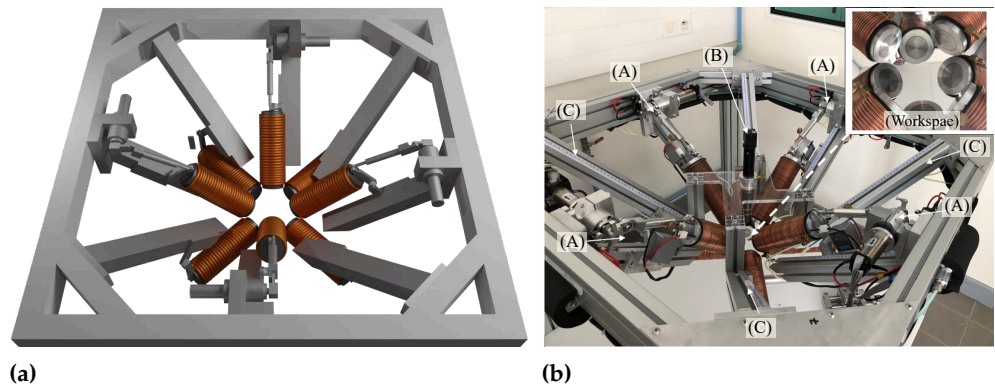


**Figure 13.** OctoRob design. (a) CAD representation of the EMA platform and (b) experimental prototype: (A) 1-DOD mobile robotic arms; (B) optical microscope with a CCD camera; (C) stationary robotic arms.

During the design process, we paid particular attention with the rigidity of the setup due to the long fixed and moving parts which have direct consequences on micromanipulation accuracy of the microrobotic tool. To deal with these constraints, the robotic arms are rigidly fixed to the frame reference structure to avoid mechanical vibrations to be transmitted to the end-effectors. Furthermore, mechanical deformations of robotic arms linked to external forces have been mechanically reinforced. When the robotic platform has been assembled, the robotic arms axes are calibrated in order to ensure that a unique point  $O$  is settled at the center of the workspace. The calibration process is based on a laser pointing system where eight laser spots are pointing towards the same focusing point  $O$  with few micrometer accuracy. The geometrical design rules have been respected during the design

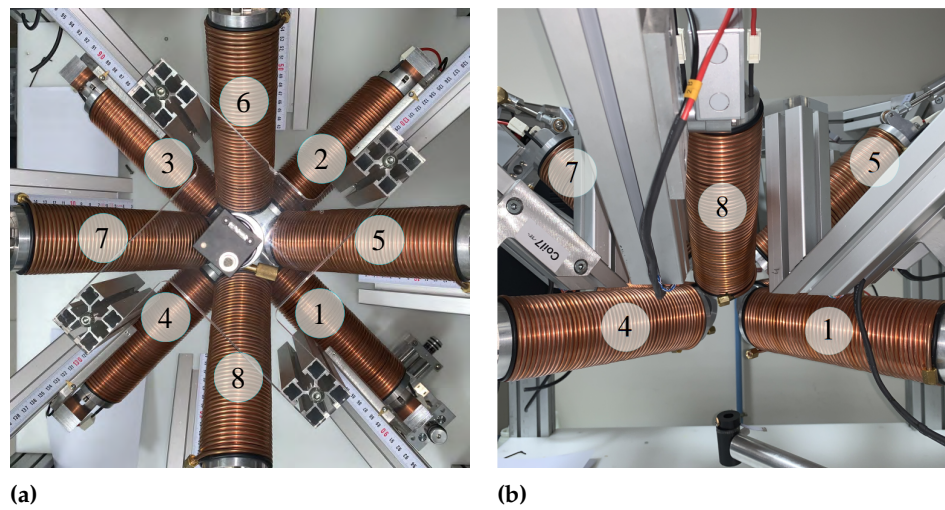


**Figure 14.** Photograph of the (a) top-view and (b) sideview of OctoRob prototype.

stage in order to have a semi-hemispherical workspace of  $45\text{mm} \times 45\text{mm} \times 45\text{mm}$ . As shown in the inset of Figure 13b, the limits of semi-hemispherical workspace are prone of any collisions: 1) the optical microscope has direct access to the workspace to provide a top-view of the eyeball, 2) the magnetic coils do not contact each other, and 3) the orientation of the mobile coils are limited by mechanical stops. Figure 14 shows closed-views of the OctoRob prototype. In the current configuration, the stationary coils have their polar angles fixed to  $\beta_i = 0$  as the OctoMag setup. If necessary, these polar angles can be modified to other configurations, for instance to  $\beta_i = 26^\circ$  as the MiniMag configuration.

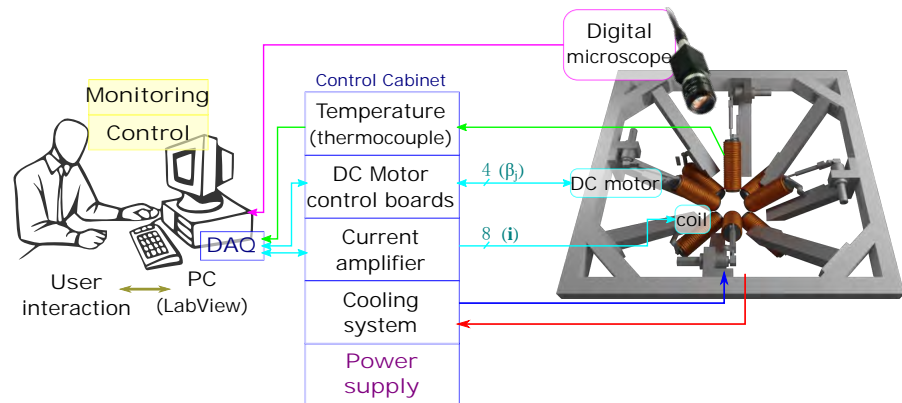


**Figure 15.** Synoptic of OctoRob platform architecture.

Figure 15 shows the overall system architecture of the OctoRob platform, which is divided in power, driving, cooling and sensing units. The current for the eight electromagnetic coils is sourced through custom-designed switched amplifiers with a maximum current of 10A per channel and controlled through two data acquisition (DAQ) card (NI PCI-6229, NI) with 12-bit resolution. The current flowing through each channel is controlled through PID controllers (Epos2 50/2 Maxon) within a range of  $-10\text{A}$  to  $10\text{A}$ . However, heat dissipation poses the limit to the maximum achievable magnetic field generated by each electromagnet. We developed then a custom cooling system capable of circulating a coolant through the copper tubing wrapped around each coil shown in Figure 16. The temperature of coil windings is monitored through temperature thermocouple sensors ( $-40^\circ$  up to  $+100^\circ\text{C}$  Radial lead, UK) integrated at the center of the coil between the spool and the winding.

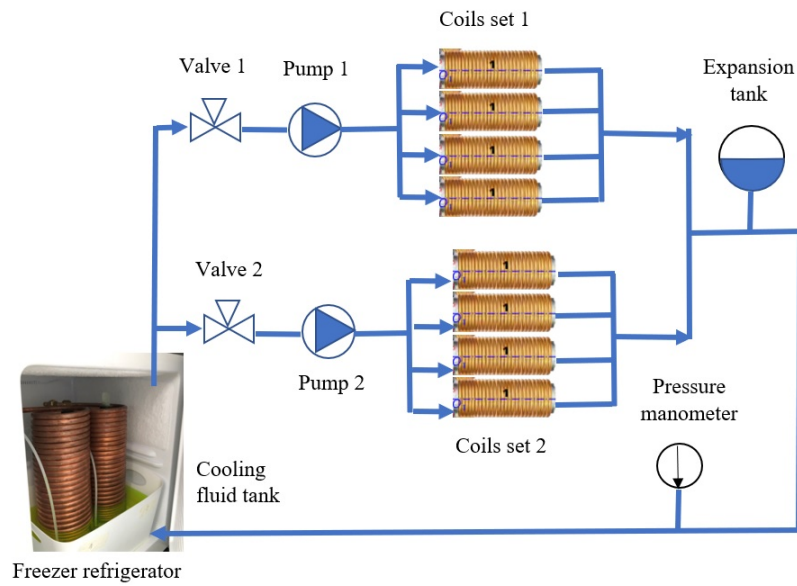


**Figure 16.** Cooling system for temperature control of electromagnets.

The four mobile robotic arms are actuated by DC motors (MDP DCX32L, France). A stationary vision system provides visual feedback of the top view of the workspace. The vision system is composed of an optical microscope (M Plan APO SL 100X, Edmund Optics, USA) connected to a digital CMOS camera delivering images and real-time video. The working distance of 90 mm with a limited depth-of-field of few tens of mm to image microrobots and a frame size of  $640 \times 480$  pixels. Since the interior of the human eye is externally observable by optical microscopy, computer vision algorithms have been developed for intraocular localization using OpenCV library. The entire system is controlled through LabView<sup>®</sup> software<sup>11</sup> environment connected to Matlab<sup>®</sup> software<sup>12</sup> by a single computer with an Intel<sup>®</sup> Core 4 Quad CPU 3.0 GHz.

## 5. Evaluation of OctoRob

The configuration of the OctoRob system should be designed in regard to the considered application, that is an ophthalmic MIS procedure. To evaluate its performance, further simulations and characterization are carried out.

### 5.1. Magnetic field and gradient of OctoRob platform

To evaluate the magnetic performance of the OctoRob we use, here, the average  $\langle \varphi \rangle$  and the uniformity  $\gamma(\varphi)$  metrics defined as follows [2]:

$$\langle \varphi \rangle = \frac{1}{N} \sum_{\mathbf{p} \in \Omega} \varphi(\mathbf{p}) \quad (7)$$

$$\gamma(\varphi) = 1 - \frac{1}{2N\langle \varphi \rangle} \sum_{\mathbf{p} \in \Omega} |\varphi(\mathbf{p}) - \langle \varphi \rangle| \quad (\text{in } \%) \quad (8)$$

where  $N$  is the number of samples and  $\varphi$  is either the magnetic field or its gradient.

As represented in Figure 14, the four stationary electromagnets ( $e = 1, 2, 3, 4$ ) are considered on the common  $xy$ -plane, and behave similarly to a Maxwell coils pairs. The left four mobile electromagnets ( $e = 5, 6, 7, 8$ ) are actuated by robotic arms described in Section 3.3. Different cases are investigated hereafter.

<sup>11</sup> <http://www.ni.com/labview/>

<sup>12</sup> <http://fr.mathworks.com>

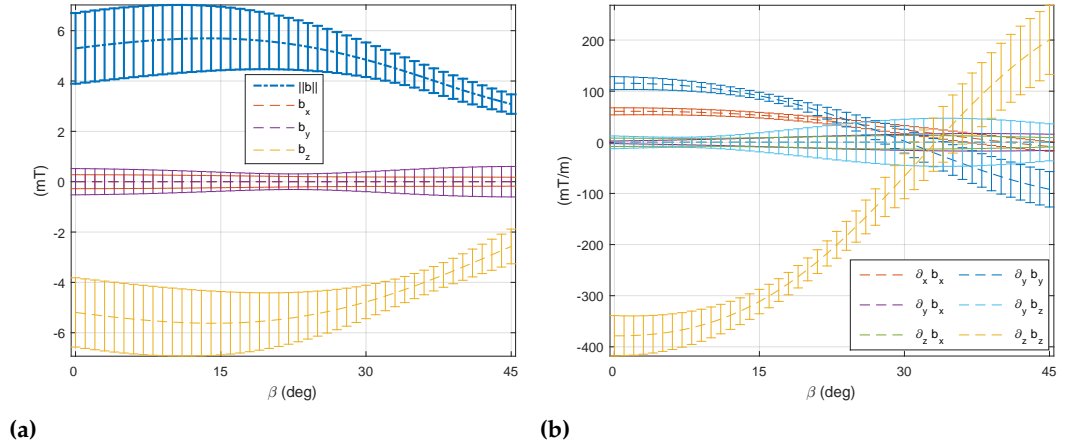


**Figure 17.** The average  $\langle \varphi \rangle$  of the (a) magnetic fields and (b) its magnetic gradients with four moving electromagnets rotating with angle  $\beta \in [0^\circ, 45^\circ]$ . The error bar shows the standard deviation of the value.

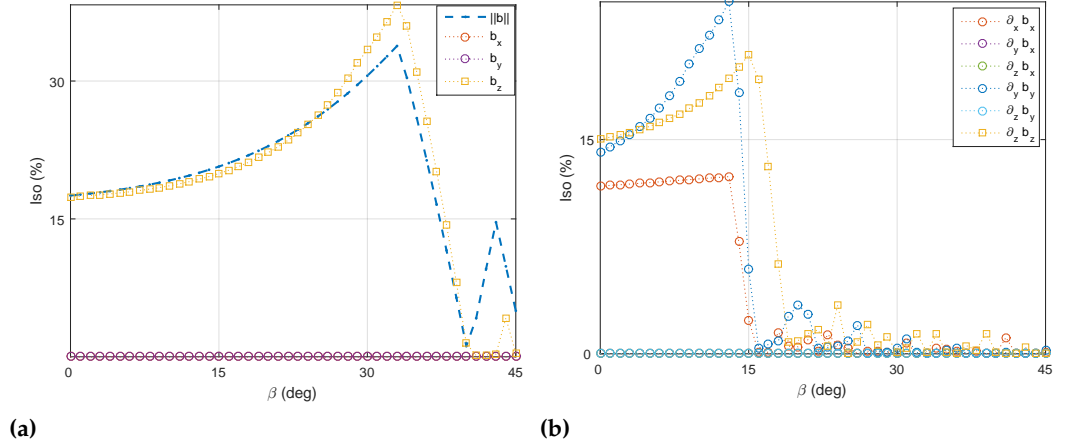


**Figure 18.** The uniformity  $\gamma(\varphi)$  of (a) magnetic fields and (b) its magnetic gradients with four moving electromagnets rotating with angle  $\beta \in [0^\circ, 45^\circ]$ .

1) The four mobile coils rotation: We first consider that the four mobile electromagnets ( $e = 5, 6, 7, 8$ ) are operated in the same way that each mobile coil is rotating together with the same angle  $\beta$ . On this basis, the optimal angle  $\beta$  is investigated to perform different manipulation tasks using either the magnetic field or its gradient. Figures 17 and 18 show the evaluation of the average (7) and uniformity (8) metrics of the magnetic field and its gradient for the rotating angle  $\beta \in [0^\circ, 45^\circ]$ . From these results, two distinguishing behaviors appear: i) magnetic field is significant enough and more uniform for mobile angle around  $\beta = 33^\circ$ ; whereas ii) a strong and uniform magnetic gradient appears at  $\beta = 14^\circ$ . Therefore, these results demonstrate the need to control either the magnetic field or its gradient by simply adjusting the orientation of certain electromagnets of the OctoRob platform to get a reliable field in the workspace.

2) A single mobile coil rotation: We here investigate the influence of having a single electromagnet ( $e = 5$ ) allowed to rotate, whereas the other mobile coils ( $e = 6, 7, 8$ ) are fixed. The four stationary electromagnets ( $e = 1, 2, 3, 4$ ) remain unchanged in the  $xy$ -plane. As mentioned, for  $\beta = 33^\circ$ , the magnetic field is more efficient. Thus, at first the mobile coils are fixed to  $33^\circ$ , and only one coil is rotating. Figure 19 describe the averages strength and the uniformity of the magnetic field in the workspace. Although the magnetic field strength does not change significantly with the rotating angle, a more uniform magnetic

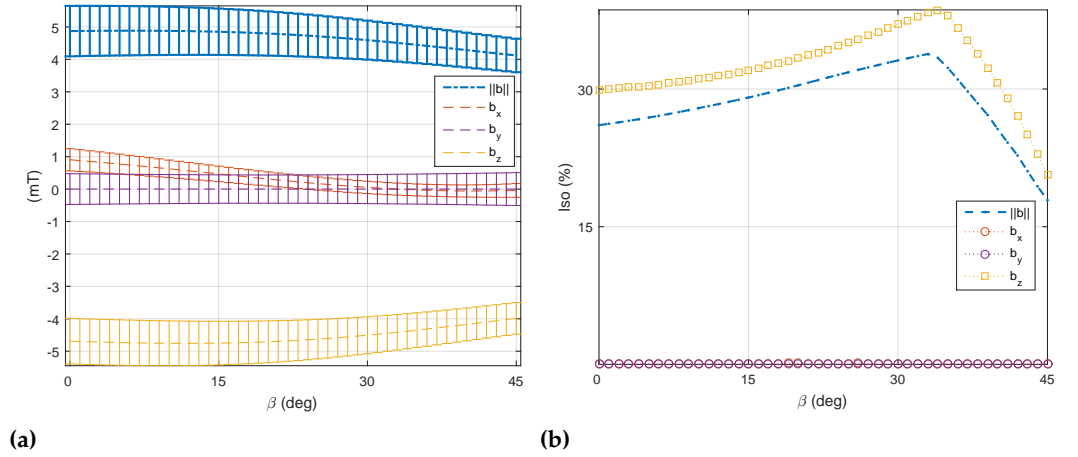


**Figure 19.** One mobile electromagnet (coil 5) is rotating and the others are set to  $\beta = 33^\circ$ : (a) the average and (b) the uniformity of the magnetic field.

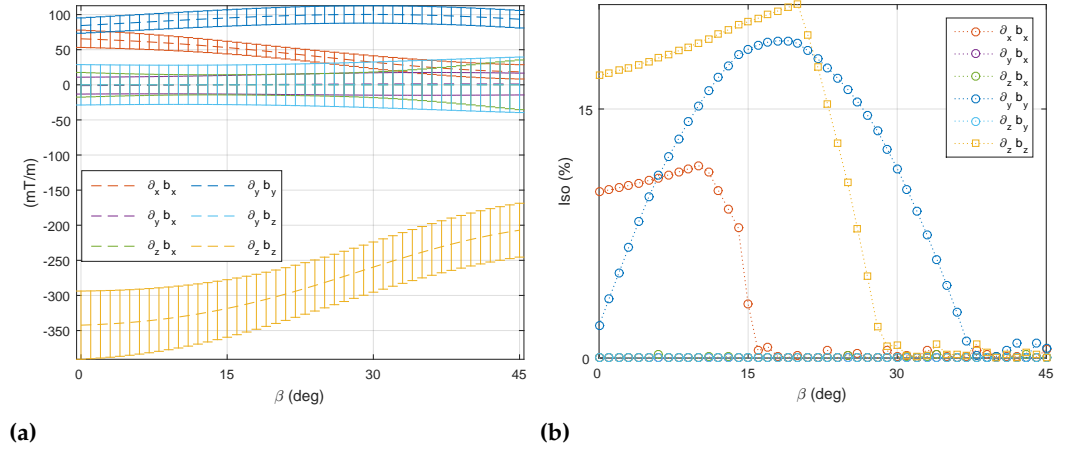


**Figure 20.** One mobile electromagnet (coil 5) is rotating and others are fixed to  $\beta = 14^\circ$ : (a) the average and (b) the uniformity of magnetic gradients.

field appears at around  $35^\circ$ . Secondly, the magnetic gradient field remains more efficient when  $\beta = 14^\circ$ . Figure 20 illustrates the average strength and their uniformity of the magnetic gradients within the workspace. The Figure 20a reveals the magnetic gradient become stronger when the mobile angle is below  $20^\circ$ . Moreover, to get more uniform magnetic gradients, it requires rotating the single coil in the range of  $5^\circ$  to  $25^\circ$ . Thus, the mobile angles  $\beta \in [5^\circ, 20^\circ]$  can be used for the more effective force control on magnetized microrobots.

3) A dual mobile coils rotation: Commonly, electromagnetic coils are used by pair. Hence, a pair of mobile coils that are opposite each other (see coil 5 and coil 7 in Figure 14) are here allowed to rotate with the same angle  $\beta \in [0^\circ, 45^\circ]$ , while the other mobile coils remain stationary. In such case, the performance of medical EMA system can be adapted by one pair of robotic arms. As previously described, the unchanged mobile coils ( $e = 5, 7$ ) are firstly fixed to  $33^\circ$  to favor the magnetic field. Figure 21 reports the performance metrics of the magnetic field, when only a pair of opposite electromagnets is rotating. Next, the fixed mobile coils ( $e = 6, 8$ ) are set to  $14^\circ$  to favor the magnetic gradient. Figure 22 illustrates the corresponding performance indicators of the magnetic gradient. As we can see, the influence of the mobile electromagnet pair is quite similar to the result of one single mobile electromagnet.

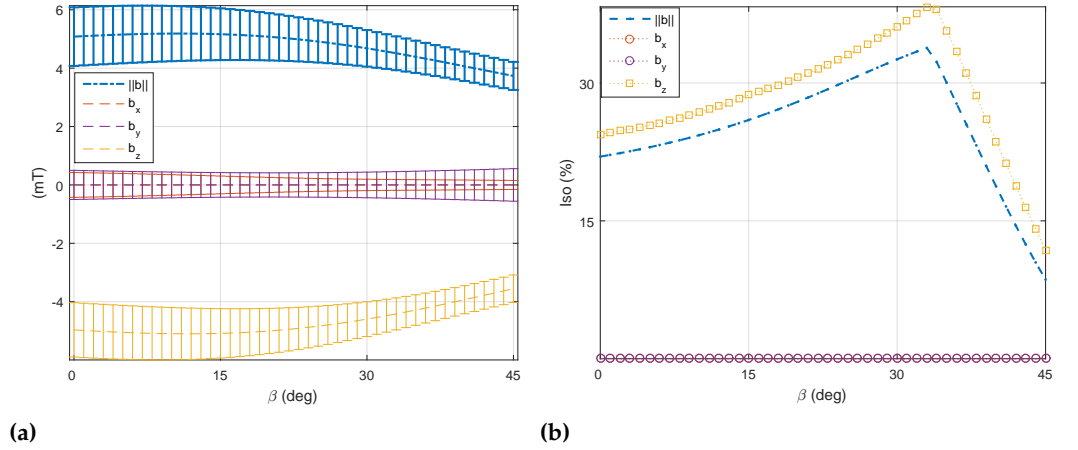


**Figure 21.** Two mobile electromagnets (dual coils 5 and 7) are rotating and the other coils set to  $\beta = 33^\circ$ :(a) the average and (b) the uniformity of the magnetic field.

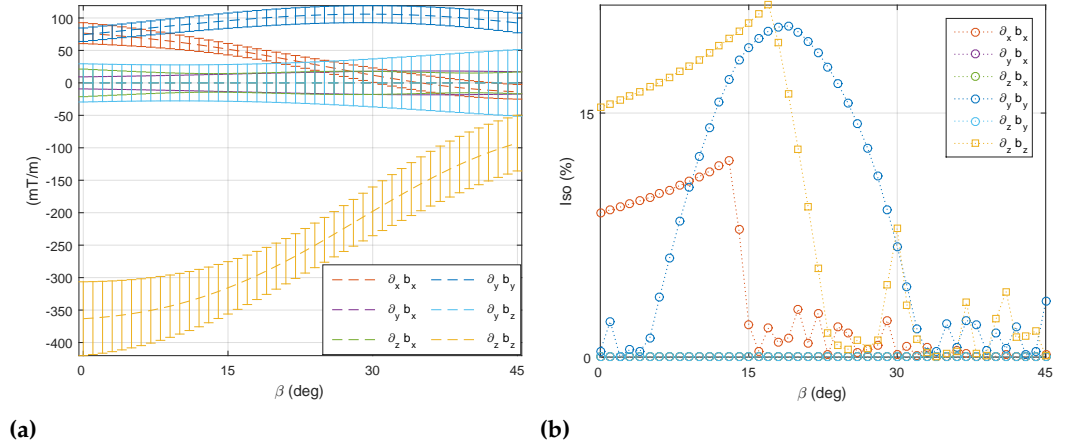


**Figure 22.** Two mobile electromagnets (dual coils 5 and 7) are rotating and the other coils set to  $\beta = 14^\circ$ :(a) the average and (b) the uniformity of the magnetic gradient.

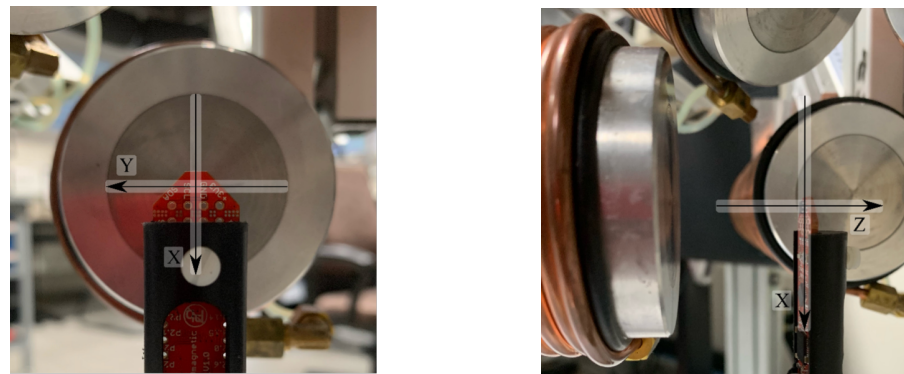
## 5.2. System characterization

The concept design of OctoRob is based on the assumption that the use of high-performance soft-magnetic material in the coils cores lead to a linear behavior regarding the input currents. Thus, the core filled in the coil is operated within its linear region (see also Figure 5). To assess this assumption, a magnetic sensor (TLE493D-MS2GO, Infineon) is placed in the center of workspace frame  $\mathcal{F}_0$ , as in the Figure 23. For the coil  $e = 1$ , the Figure 24 shows the measured magnetic field. These results confirm that the electromagnetic coil works in the linear region. The evaluated linear coefficients are reported in the Table 3.

**Table 3.** Linear coefficient between magnetic field and input current for each coil.

	Coil1	Coil2	Coil3	Coil4	Coil5	Coil6	Coil7	Coil8
$k_x$	0.416	0.4176	-0.2981	-0.3506	-1.3067	0.0102	1.1860	-0.1290
$k_y$	-0.5723	0.3588	0.3375	-0.3331	0.0496	1.3262	-0.0875	-1.3181
$k_z$	-0.3204	-0.7325	-0.4108	-0.4529	0.1263	0.0760	0.1347	0.1263

As mentioned above, a unit-current field map must be constructed for each of the electromagnets. An analytical model is chosen to fit the magnetic field data obtained by a finite element method for the unit-current contributions. The point-dipole model Eq. (1) is



(a)

(b)

**Figure 23.** The definition of the magnetic directions  $x$ ,  $y$ ,  $z$  of the sensor TLE493D-W2B6. 23a the front view of magnetic sensor; 23b the side view of magnetic sensor.

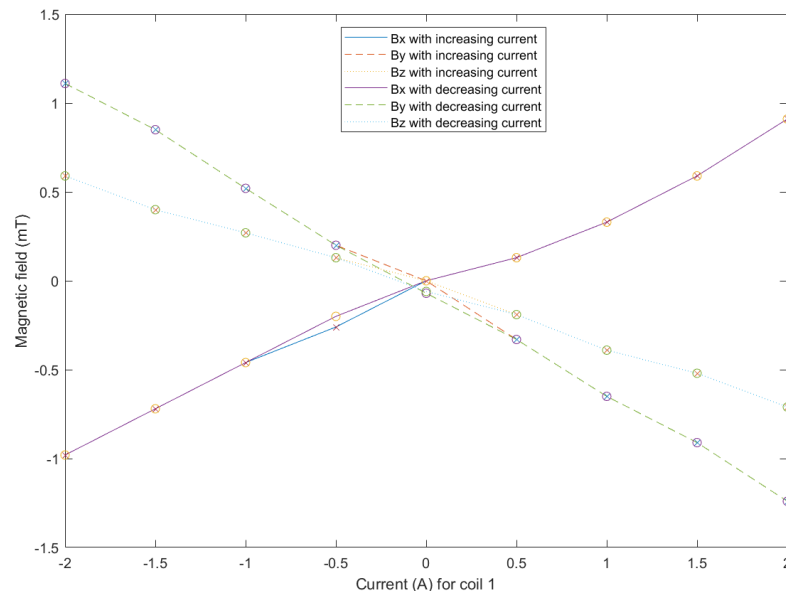


**Figure 24.** Hysteresis curve for the magnetic field at the center of the workspace as a function of current ( $-2\text{A}$  to  $2\text{A}$ ) actuating the coil 1. The shape  $x$  in the curve denotes the data for increasing current and shape  $o$  denotes the data for decreasing current.

derived to apply the computation of magnetic fields. Figure 25 shows the magnetic field strength along the  $x$ -axis of the electromagnet  $e$  computed from Eq. (1) and measured with the magnetic sensor. As one can see, the theoretical values obtained using the point-dipole model become close to the measured values for location between 50 mm to 70 mm to the coil center, as reported in the Figure 25b. When the working distance  $d_w$  is adjusted between 50 mm to 70 mm, the relative error is less 10% as presented in the Figure 25d. This reinforces the choice of the distance  $d_w = 65$  mm resulting from the specifications indicated in Section 2.2.

After calibration, the Figure 26 presents that the magnetic fields generated by the OctoRob platform behave linearly with respect to the input currents flowing through the electromagnets (four coils  $e = 1, 2, 3, 4$ ), and the currents from 0A to 3A have been applied.

### 5.3. Discussions

The OctoRob platform is designed based on the previous analysis of different EMA arrangements [2]. Globally, it appears that most EMA system exhibits different magnetic performance for different positions and orientations of their coils. Hence, the built robotized

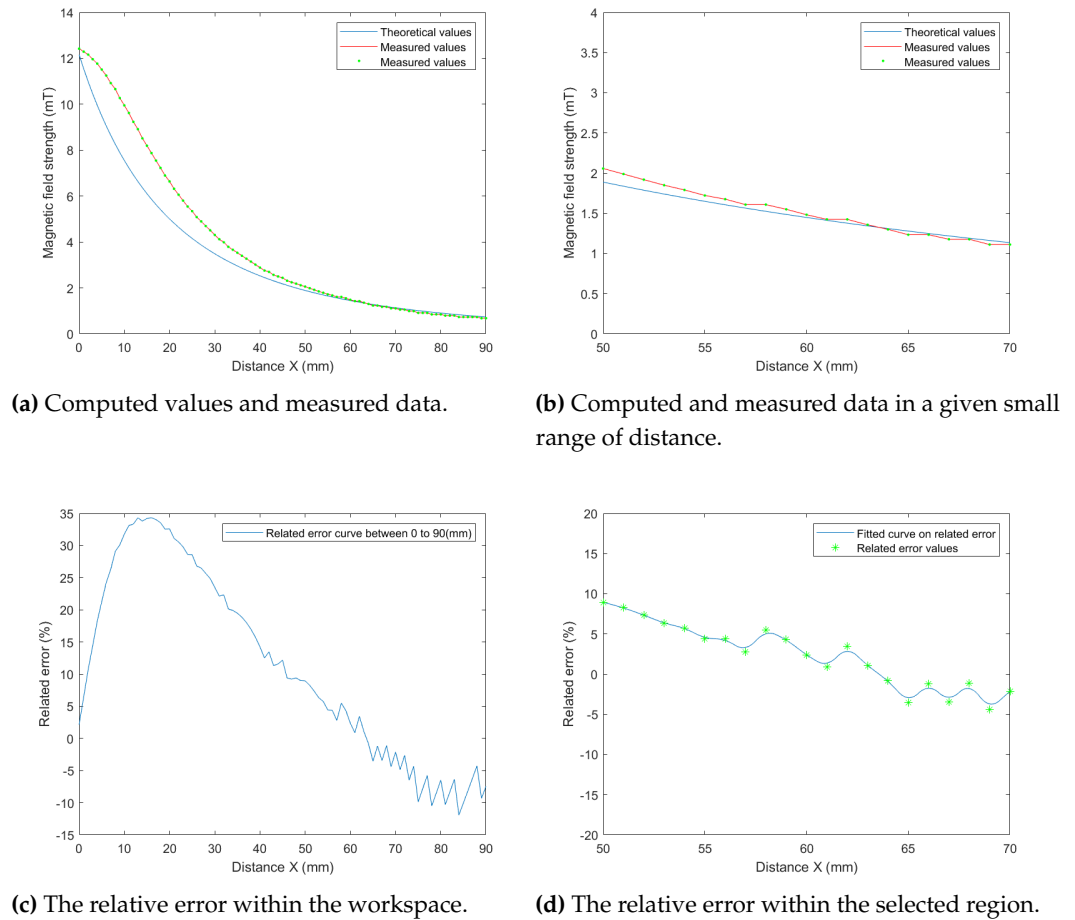


**Figure 25.** Comparison of theoretical values and measured values of magnetic field: (a) magnetic field strength along the symmetry axis (x-axis) of the electromagnet, and comparison of theoretical values and measured values. The detected locations are selected from 0 mm to 90 mm in the measurement and (b) the detected locations are selected from 50 mm to 70 mm in the measurement; (c)-(d) the relative error within the workspace. The detected locations are selected from 0 mm to 90 mm and from 50 mm to 70 mm in the measurement, respectively.

OctoRob system comprises two sets of coils: four fixed electromagnets and four mobile electromagnets. The results indicate that the high moving angle (around  $\beta = 33^\circ$ ) is most suitable to generate a strong and uniform magnetic field. A most strong and uniform magnetic gradient field can be only achieved at low moving angles  $\beta < 20^\circ$ . Since the magnetic fields induce the torque and the force is commonly generated by magnetic gradients, this study demonstrates that the designed OctoRob system provides more versatile mode for effective control of biomedical microrobots in different situations. For example, the helical microswimmer could be propelled through the VH using a rotating magnetic field, then through magnetic gradient manipulation it could perform therapeutic tasks, such as targeted therapy and/or material removal (peeling, puncture, drug delivery, etc.). Therefore, the developed platform would assist surgeons in difficult retinal ophthalmic MIS procedures. Any similar applications where both magnetic fields and gradients are important aspects, and where the hemispherical arrangement is practical can also be considered. For example, OctoRob can be placed above certain parts of a limb (e.g. knee, arm...) or over some organs (e.g. liver, kidney...).

Furthermore, the three considered cases, discussed in Section 5.1, provide results that are similar, leading to two interesting aspects. First, we can roughly choose the most simple strategy, for instance, only one electromagnet is moving by a robotic arm. However, to

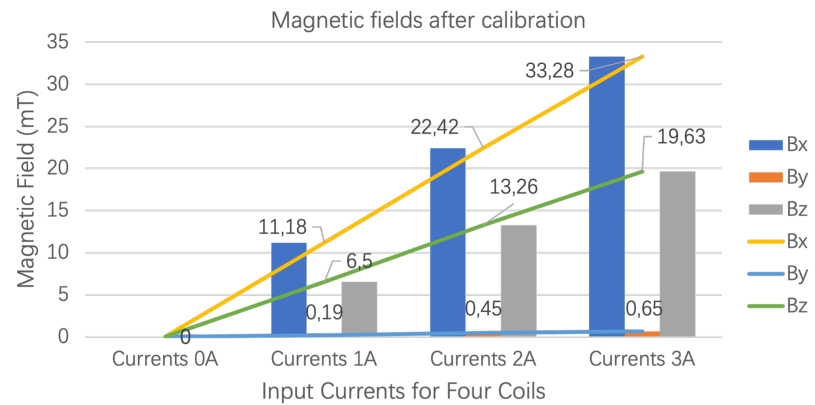


**Figure 26.** Measured magnetic fields after the calibrations in the workspace center.

achieve more precise and more efficient trajectory tracking or large magnetic force or torque, more mobile electromagnet should be considered. Secondly, the results also suggest that the moving coils do not necessarily need to be accurately controlled to enable either good magnetic field or gradient capability.

## 6. Conclusion

This paper presents the development of a novel robotized OctoRob system with an initial motivation to improve ophthalmic procedures with untethered biomedical magnetic microrobots. Previous studies have shown that the designed EMA platform must be defined with respect to the considered application. Hence, from the analysis of the specificities of ophthalmic operations, the OctoRob specifications are defined. The proposed EMA system includes four static electromagnets and four robotized electromagnets allowing sometimes to favor the magnetic field sometimes its gradient. The coil sizing and implementation is done to provide a balance between the workspace size and the magnetic field performance. Different moving cases of the mobile electromagnets have been evaluated. The evaluation of OctoRob magnetic capability shows that the mobile electromagnets allow a variety of magnetic field distributions. Specifically, a low angle  $\beta$  leads to stronger and more uniform magnetic gradient distribution, whereas most uniform magnetic field is produced near a high mobile angle  $\beta$ . Furthermore, the system calibration has been completed to approach the designed model. The results of system characterization prove that the implemented platform works in the linear region of the generated electromagnetic fields regarding the input currents. The proposed mathematical model of magnetic field generation has also been validated through the calibration process. Therefore, the reconfigurable OctoRob platform allows providing more versatility, maneuverability and flexibility to the magnetic manipulation of biomedical microrobots to help surgeons in difficult ophthalmic surgeries. In the future, model trials regarding ophthalmic applications will be performed on this platform, and the performances of designed robotized OctoRob system will be further investigated and improved.

**Author Contributions:** Conceptualization, R.C., D.F. and A.F.; Methodology, R.C.; Analysis, R.C. and D.F.; Writing—original draft, R.C. and D.F.; Writing—review and editing, R.C., D.F. and A.F.; Project administration, A.F.; Funding Acquisition, A.F. All authors have read and agreed to the published version of the manuscript.

**Funding:** This work was supported by the Region Centre Val de Loire funding, project: BUBBLEBOT.

**Institutional Review Board Statement:** Not applicable.

**Informed Consent Statement:** Not applicable.

**Data Availability Statement:** The data presented in this study are available from the corresponding authors upon reasonable request.

**Acknowledgments:** This work was supported by French National Institute of Health and Medical Research (Inserm) “Plan Cancer” program and the Microrobots Targeting Glioblastoma (MTG) project.

**Conflicts of Interest:** The authors declare no conflict of interest.

**Sample Availability:** Not applicable.

## Abbreviations

The following abbreviations are used in this manuscript:

DOF	degree of freedom
EMA	Electromagnetic actuation
MIS	minimally invasive surgery
VH	vitreous humor
LD	Linear dichroism
FEM	Finite Element Method
FEA	Finite Element Analysis
PID	Proportional Integral Derivative
DAQ	Data Acquisition
DC	Direct Current

## Appendix A

### Appendix A.1 Coordinate transformation

In robotics applications, many different coordinate systems can be used to define where robots, sensors, and other objects are located [42]. In general, the location of a body in 3D space can be specified by its position and orientation. There are multiple possible representations for these values, some of which are specific to certain applications.

Coordinate transformation is a method of modeling the linkages and joints of a mechanism. Hence, a frame  $\mathcal{F}_0$  is attached to each link of the robotic system. Then, homogeneous transformation is used to describe the spatial relationship between the two adjacent links. Through the sequential transformation, the pose (i.e. the position and orientation) of the end-effector relative to the reference frame  $\mathcal{F}_0$  can be finally derived thereby to establish the kinematic equation of the robotic arm. Commonly, each joint of the robot can only achieve a form of motion, such as rotation or translation. Therefore, the mechanical arm joint is divided as either hinged or sliding joints. For the OctoRob EMA platform, currently, only<sup>13</sup> rotational motion of the robotic arm is defined. The designed electromagnetic coil is fixed on the end-effector of the robotic arm.

### Appendix A.2 Definition of transformation matrices

The pose of the end-effector are obtained by Cartesian space transformation of the joints of the robotic arm. This pose of the end-effector relative to the reference  $\mathcal{F}_0$  can be computed by the given set of joint angles and links length. The direct geometric model of OctoRob robotic arm, recalled in Figure A1, includes here the following steps: First, the pose ( $C$  and  $F$ ) of the fixed link is characterized in the reference  $\mathcal{F}_0$ . Second, the transformation matrix related to the active joint  $\theta_1$  is established. Thus, the offset angle (namely the Denavit–Hartenberg parameters) between two adjacent links should be determined. Third, the coordinate transformation can be defined by the product of each transformation matrices, including their rotation and the translation matrices. Last, the all transformation matrices are applied from the fixed pose to obtain the pose of the end-effector  $H$  in  $\mathcal{F}_0$ .

<sup>13</sup> The distance between the electromagnet and the workspace center is also affected by the rotation motion by motor.

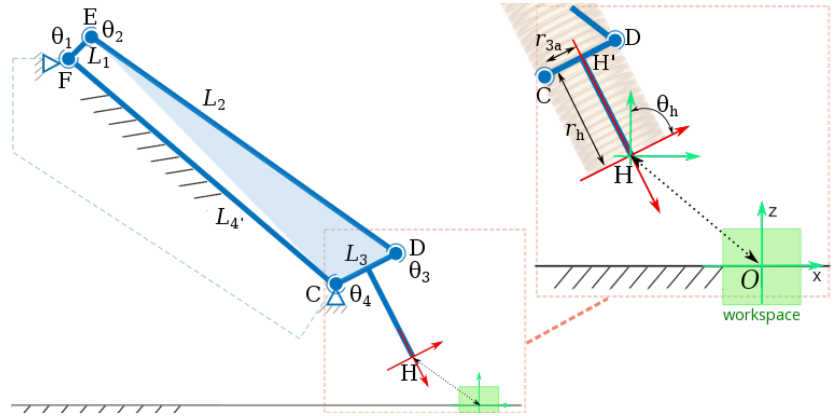


**Figure A1.** Representation of the robotic arm kinematics chain with the four links  $L_1$ - $L_4$  and joints  $\theta_1$ - $\theta_4$ .

Furthermore, the inverse geometric model means the calculation of the each joint angle  $\theta_i$  of the robotic arm from the given pose of the end-effector described by Cartesian coordinate system. The inverse geometric model is actually multi-solvent, that is, a specific status of the end-effector can be achieved in various combinations of the robotic joint angles, and the solution of inverse geometric is usually difficult to determine.

Finally, the pose accuracy and repeated precision have been considered in the measure. The positioning accuracy is used as an indicator of ability for achieving a Cartesian coordinate system by the provided joint angle of robotic arm using the direct geometric model. Besides the repeatability precision presents the capability for manipulation of the end-effector in a given Cartesian coordinate system by using the inverse geometry. Usually, the repeatability precision of the robotic arm is great while the positioning accuracy is poor. Therefore, such effect of movement should be considered in the designing process of robotic arm.

### Appendix A.3 Rotation matrix

The rotation matrix can be used to rotate the frame linked to an object in Euclidean space. The rotation matrix determines its sign by using right-hand rule, which is the positive sign produced by counterclockwise rotation along its axis. Let  $\text{Rot}_x\theta$  be a pure rotation about the axis  $x$  by an angle  $\theta$ , that is basically defined as:

$$\text{Rot}_x\theta = \begin{pmatrix} 1 & 0 & 0 \\ 0 & \cos(\theta) & -\sin(\theta) \\ 0 & \sin(\theta) & \cos(\theta) \end{pmatrix} \quad (\text{A1})$$

For 3D rotation transformation, it remains to define the pure rotation about the  $y$  and  $z$ -axis, and we get:

$$\text{Rot}_y\theta = \begin{pmatrix} \cos(\theta) & 0 & \sin(\theta) \\ 0 & 1 & 0 \\ -\sin(\theta) & 0 & \cos(\theta) \end{pmatrix} \quad (\text{A2})$$

$$\text{Rot}_z\theta = \begin{pmatrix} \cos(\theta) & -\sin(\theta) & 0 \\ \sin(\theta) & \cos(\theta) & 0 \\ 0 & 0 & 1 \end{pmatrix} \quad (\text{A3})$$

These basic rotation matrices can apply directly to the general rotations. In the 3D coordinate, the general rotation matrix can be obtained by the following equation:

$$\mathbf{R}(\alpha, \beta, \gamma) = \text{Rot}_z\alpha\text{Rot}_y\beta\text{Rot}_x\gamma \quad (\text{A4})$$

where  $\alpha$ ,  $\beta$  and  $\gamma$  represents rotation yaw, pitch and roll angles about axes  $z$ ,  $y$  and  $x$ , respectively.

Commonly, it is more convenient to define and utilize global rotation matrix  $\mathbf{R}(\alpha, \beta, \gamma)$ . For instance, when a vector  $\mathbf{p}$  is rotated with a sole angle  $\theta$  along a arbitrary vector, the following steps can be used for the computation to obtain the transformation matrix. Let consider the rotation of a vector given as  $\mathbf{p} = [a_2 - a_1, b_2 - b_1, c_2 - c_1] = [a, b, c]$ , that is illustrated in Figure A2a. In the Figure A2b, the rotation axis is translated to the origin coordinate  $O$  as step 1. The step 2 is the operation to rotate the rotation axis to the  $yoz$ -plane as shown in the Figure A2c. Then the axis of rotation is rotated to coincide with  $z$ -axis as step3 shown in the Figure A2d. After finishing the above three steps, the object is rotated with  $\theta$  degree along  $z$ -axis. Furthermore, the reverse processes of step 3, step 2 and step 1 should be performed respectively to complete this rotation process.

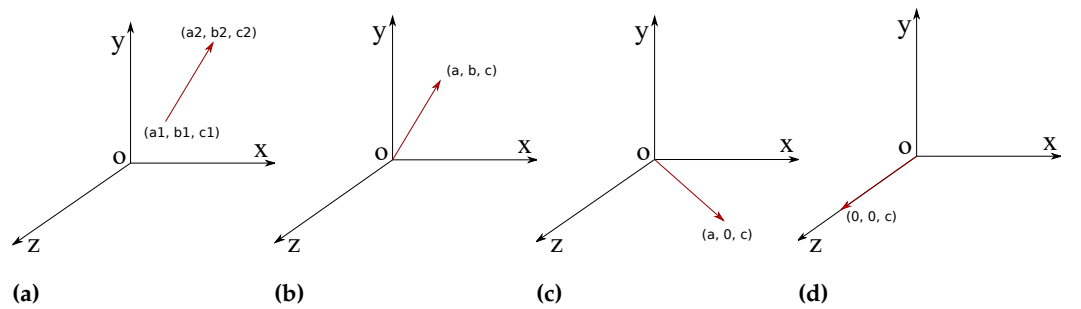


**Figure A2.** Illustration of rotation step along a vector axis. A vector is referred as rotation axis in (a); (b): translate the rotation axis to origin coordinate; (c): rotate the rotation axis to  $yoz$ -plane; (d): rotate the rotation axis to coincide with  $z$ -axis. Then the object can be rotated angle  $\theta$  along  $z$ -axis.

#### Appendix A.4 Transformation matrix of a pure translation

These operations can be expressed by the transformation matrix composed of translation matrix and rotation matrices. Transformation matrix of a pure translation is defined with homogeneous coordinate as:

$$\text{Trans}(a, b, c) = \begin{pmatrix} 1 & 0 & 0 & a \\ 0 & 1 & 0 & b \\ 0 & 0 & 1 & c \\ 0 & 0 & 0 & 1 \end{pmatrix} \quad (\text{A5})$$

with  $a$ ,  $b$ , and  $c$  the translation along the  $x$ ,  $y$  and  $z$  axes respectively. We will also use the notation  $\text{Trans}_x(a)$  to denote the pure translation along the  $x$ -axis by a value  $a$ .

#### Appendix A.5 Homogeneous transformation matrices

Let  $\mathbf{p} = [a, b, c]$  be a vector, as illustrated in the Figure A3. The rotation matrix  $\text{Rot}_x\gamma$  is defined for the rotational operation of the vector axis along the  $x$ -axis to the  $xOz$ -plane, that is:

$$\text{Rot}_x\theta(\gamma) = \begin{pmatrix} 1 & 0 & 0 & 0 \\ 0 & \cos(\gamma) & -\sin(\gamma) & 0 \\ 0 & \sin(\gamma) & \cos(\gamma) & 0 \\ 0 & 0 & 0 & 1 \end{pmatrix} = \begin{pmatrix} 1 & 0 & 0 & 0 \\ 0 & \frac{c}{\sqrt{b^2+c^2}} & -\frac{b}{\sqrt{b^2+c^2}} & 0 \\ 0 & \frac{b}{\sqrt{b^2+c^2}} & \frac{c}{\sqrt{b^2+c^2}} & 0 \\ 0 & 0 & 0 & 1 \end{pmatrix} \quad (\text{A6})$$

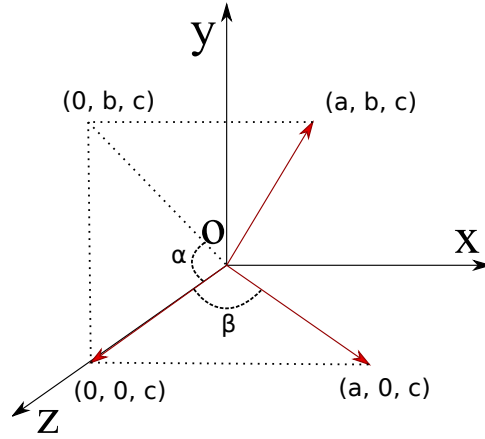


**Figure A3.** The illustration of the angles between vector axis and coordinate axes.

The vector axis is rotated along the  $y$ -axis to coincide with the  $z$ -axis on  $xOz$ -plane by the following rotation matrix:

$$\text{Rot}_{y-\beta} = \begin{pmatrix} \cos(-\beta) & 0 & \sin(-\beta) & 0 \\ 0 & 1 & 0 & 0 \\ -\sin(-\beta) & 0 & \cos(-\beta) & 0 \\ 0 & 0 & 0 & 1 \end{pmatrix} = \begin{pmatrix} \frac{\sqrt{b^2+c^2}}{\sqrt{a^2+b^2+c^2}} & 0 & -\frac{a}{\sqrt{a^2+b^2+c^2}} & 0 \\ 0 & 1 & 0 & 0 \\ \frac{a}{\sqrt{a^2+b^2+c^2}} & 0 & \frac{\sqrt{b^2+c^2}}{\sqrt{a^2+b^2+c^2}} & 0 \\ 0 & 0 & 0 & 1 \end{pmatrix} \quad (\text{A7})$$

Let us note that the angle of rotation matrix is here negative due to vector axis is rotating clockwise around the  $y$ -axis. Finally, since the arbitrary rotation axis and  $z$ -axis coincide, the vector can be rotated with the angle  $\alpha$  around the  $z$ -axis by applying:

$$\text{Rot}_z\alpha = \begin{pmatrix} \cos(\alpha) & -\sin(\alpha) & 0 & 0 \\ \sin(\alpha) & \cos(\alpha) & 0 & 0 \\ 0 & 0 & 1 & 0 \\ 0 & 0 & 0 & 1 \end{pmatrix} \quad (\text{A8})$$

When rotation axis is connected to origin  $O$ , the rotational transformation matrix is computed from step 2, here, without translation. Wherefore the transformation matrix can be calculated as followings:

$$\mathbf{T}_{\text{rot}} = \text{Rot}_x(-\gamma)\text{Rot}_y(\beta)\text{Rot}_z(-\alpha)\text{Rot}_x(\gamma) \quad (\text{A9})$$

where the matrix  $\mathbf{T}$  should be used for left multiplication of the vector, that is  $\mathbf{p}' = \mathbf{T}_{\text{rot}}\mathbf{p}$ . The equations of each step are substituted into the Figure A9 to obtained the global transformation:

$$\mathbf{T}_{\text{rot}} = \begin{pmatrix} a^2 + (1 - a^2) \cos(\theta) & ab(1 - \cos(\theta)) - c \sin(\theta) & ac(1 - \cos(\theta)) + b \sin(\theta) & 0 \\ ab(1 - \cos(\theta)) + c \sin(\theta) & b^2 + (1 - b^2) \cos(\theta) & bc(1 - \cos(\theta)) - a \sin(\theta) & 0 \\ ac(1 - \cos(\theta)) - b \sin(\theta) & bc(1 - \cos(\theta)) + a \sin(\theta) & c^2 + (1 - c^2) \cos(\theta) & 0 \\ 0 & 0 & 0 & 1 \end{pmatrix} \quad (\text{A10})$$

If the vector  $\mathbf{p}$  is not on the origin  $O$  of the frame, as in Figure A2a, the first translation and last reverse operation can not be omitted. The transformation matrix is consequently derived from:

$$\mathbf{T} = \text{Trans}(-a_1, -b_1, -c_1)\mathbf{T}_{\text{rot}}\text{Trans}(a_1, b_1, c_1) \quad (\text{A11})$$

where  $(a_1, b_1, c_1)$  denotes the origin of the vector  $\mathbf{p}$ . Therefore, the final transformation matrix is expressed as:

$$\mathbf{T} = \begin{pmatrix} a^2 + bc \cos(\theta) & ab\zeta - c \sin(\theta) & ac\zeta + b \sin(\theta) & (a_1bc - a(b_1b + c_1c))\zeta + (b_1c - c_1b) \sin(\theta) \\ ab\zeta + c \sin(\theta) & b^2 + ac \cos(\theta) & bc\zeta - b \sin(\theta) & (b_1ac - b(a_1a + c_1c))\zeta + (c_1a - a_1c) \sin(\theta) \\ ac\zeta - b \sin(\theta) & bc\zeta + a \sin(\theta) & c^2 + ab \cos(\theta) & (c_1ab - c(a_1a + b_1b))\zeta + (a_1b - b_1a) \sin(\theta) \\ 0 & 0 & 0 & 1 \end{pmatrix} \quad (\text{A12})$$

with  $\zeta = (1 - \cos(\theta))$ ;  $ab = (a^2 + b^2)$ ,  $ac = (a^2 + c^2)$  and  $bc = (b^2 + c^2)$ .

The resulting homogeneous transformation matrix can be used to obtain the positions and orientations of the electromagnets, for the mechanical design of the robotic arms as well.

## References

1. Chautems, C.; Zeydan, B.; Charreyron, S.; Chatzipirpiridis, G.; Pané, S.; Nelson, B.J. Magnetically powered microrobots: a medical revolution underway? *European Journal of Cardio-Thoracic Surgery*, 51, 405–407. doi:10.1093/ejcts/ezw432.
2. Chen, R.; Folio, D.; Ferreira, A. Mathematical approach for the design configuration of magnetic system with multiple electromagnets. *Robotics and Autonomous Systems* **2021**, 135, 103674.
3. Chen, R.; Folio, D.; Ferreira, A. Analysis and Comparison of Electromagnetic Microrobotic Platforms for Biomedical Applications. *Applied Sciences* **2022**, 12, 456.
4. Kummer, M.P.; Abbott, J.J.; Kratochvil, B.E.; Borer, R.; Sengul, A.; Nelson, B.J. OctoMag: An electromagnetic system for 5-DOF wireless micromanipulation. *IEEE Trans. Robot.* **2010**, 26, 1006–1017.
5. Gupta, P.K.; Jensen, P.S.; de Juan, E. Surgical forces and tactile perception during retinal microsurgery. International conference on medical image computing and computer-assisted intervention. Springer International Publishing, 1999, pp. 1218–1225.
6. Jagtap, A.D.; Riviere, C.N. Applied force during vitreoretinal microsurgery with handheld instruments. Annual International Conference of the IEEE Engineering in Medicine and Biology Society. IEEE, 2004, Vol. 1, pp. 2771–2773.
7. Singhy, S.; Riviere, C. Physiological tremor amplitude during retinal microsurgery. IEEE Annual Northeast Bioengineering Conference. IEEE, 2002, pp. 171–172.
8. Fine, H.F.; Wei, W.; Goldman, R.E.; Simaan, N. Robot-assisted ophthalmic surgery. *Canadian Journal of Ophthalmology* **2010**, 45, 581–584.
9. Pitcher, J.D.; Wilson, J.T.; Tsao, T.C.; Schwartz, S.D.; Hubschman, J.P. Robotic eye surgery: past, present, and future. *Journal of Computer Science & Systems Biology* **2012**, 5, 1.
10. Spandau, U.; Scharioth, G. *Cutting Edge of Ophthalmic Surgery: From Refractive SMILE to Robotic Vitrectomy*; Springer International Publishing, 2017.
11. Channa, R.; Iordachita, I.; Handa, J.T. Robotic Eye Surgery. *Retina (Philadelphia, Pa.)* **2017**, 37, 1220.
12. Zhang, L.; Abbott, J.J.; Dong, L.; Kratochvil, B.E.; Bell, D.; Nelson, B.J. Artificial bacterial flagella: Fabrication and magnetic control. *Applied Physics Letters* **2009**, 94, 064107.
13. Zhang, L.; Abbott, J.J.; Dong, L.; Peyer, K.E.; Kratochvil, B.E.; Zhang, H.; Bergeles, C.; Nelson, B.J. Characterizing the swimming properties of artificial bacterial flagella. *Nano letters* **2009**, 9, 3663–3667.
14. Zhang, L.; Peyer, K.E.; Nelson, B.J. Artificial bacterial flagella for micromanipulation. *Lab on a Chip* **2010**, 10, 2203–2215.
15. Peyer, K.E.; Zhang, L.; Nelson, B.J. Bio-inspired magnetic swimming microrobots for biomedical applications. *Nanoscale* **2013**, 5, 1259–1272.
16. Peyer, K.E.; Tottori, S.; Qiu, F.; Zhang, L.; Nelson, B.J. Magnetic helical micromachines. *Chemistry—A European Journal* **2013**, 19, 28–38.
17. Nelson, B.J.; Peyer, K.E. Micro-and nanorobots swimming in heterogeneous liquids. *ACS Nano* **2014**, 8, 8718–8724.
18. Nelson, B.J.; Kaliakatsos, I.K.; Abbott, J.J. Microrobots for minimally invasive medicine. *Annual review of biomedical engineering* **2010**, 12, 55–85.
19. Snell, R.S.; Lemp, M.A. *Clinical anatomy of the eye*; John Wiley & Sons, 2013.
20. Tang, W.M.; Han, D.P. A study of surgical approaches to retinal vascular occlusions. *Archives of Ophthalmology* **2000**, 118, 138–143.
21. Shahid, H.; Hossain, P.; Amoaku, W. The management of retinal vein occlusion: is interventional ophthalmology the way forward? *British Journal of Ophthalmology* **2006**, 90, 627–639.
22. Meredith, T.A. *Atlas of retinal and vitreous surgery*; Mosby Incorporated, 1999.
23. Bonfiglio, A.; Repetto, R.; Siggers, J.H.; Stocchino, A. Investigation of the motion of a viscous fluid in the vitreous cavity induced by eye rotations and implications for drug delivery. *Physics in Medicine & Biology* **2013**, 58, 1969.
24. Bonfiglio, A.; Lagazzo, A.; Repetto, R.; Stocchino, A. An experimental model of vitreous motion induced by eye rotations. *Eye and Vision* **2015**, 2, 10.
25. Silva, A.F.; Alves, M.A.; Oliveira, M.S.N. Rheological Behaviour of Vitreous Humour. *Rheologica Acta* **2017**, 56, 377–386. doi:10.1007/s00397-017-0997-0.
26. Purcell, E.M. Life at low Reynolds number. *American journal of physics* **1977**, 45, 3–11.
27. Bekerman, I.; Gottlieb, P.; Vaiman, M. Variations in eyeball diameters of the healthy adults. *Journal of ophthalmology* **2014**, 2014.

28. Amblard, F.; Yurke, B.; Pargellis, A.; Leibler, S. A magnetic manipulator for studying local rheology and micromechanical properties of biological systems. *Review of Scientific Instruments* **1996**, *67*, 818–827.
29. Dogangil, G.; Ergeneman, O.; Abbott, J.J.; Pané, S.; Hall, H.; Muntwyler, S.; Nelson, B.J. Toward targeted retinal drug delivery with wireless magnetic microrobots. *IEEE/RSJ International Conference on Intelligent Robots and Systems (IROS)*. IEEE, 2008, pp. 1921–1926.
30. Abolhassani, N.; Patel, R.; Moallem, M. Needle Insertion into Soft Tissue: A Survey. *Medical Engineering & Physics*, *29*, 413–431.
31. Chen, R.; Folio, D.; Ferreira, A. Performance metrics for a robotic actuation system using static and mobile electromagnets. *2019 International Conference on Robotics and Automation (ICRA)*. IEEE, 2019, pp. 2474–2480.
32. Petruska, A.J.; Nelson, B.J. Minimum bounds on the number of electromagnets required for remote magnetic manipulation. *IEEE Trans. Robot.* **2015**, *31*, 714–722.
33. Wong, D.; Steager, E.B.; Kumar, V. Independent control of identical magnetic robots in a plane. *IEEE Robotics and Automation Letters* **2016**, *1*, 554–561.
34. Etiévant, M.; Bolopion, A.; Régnier, S.; Andreff, N. An Improved Control-Oriented Modeling of the Magnetic Field. *International Conference on Robotics and Automation (ICRA)*. IEEE, 2019, pp. 6178–6184.
35. Jing, X.; Guo, W. Modeling and Configuration Design of Electromagnetic Actuation Coil for a Magnetically Controlled Microrobot. *Chinese Journal of Mechanical Engineering* **2019**, *32*, 63.
36. Furlani, E.P. *Permanent magnet and electromechanical devices: materials, analysis, and applications*; Academic press, 2001. doi:10.1016/B978-0-12-269951-1.X5000-1.
37. McCaig, M. *Permanent Magnets in Theory and Practice*; Pentech Press, 1977.
38. Woolman, J.; Mottram, R. *The mechanical and physical properties of the British Standard En steels*; Vol. 2, EN 40 TO EN 363, Pergamon Press, 1964.
39. Kummer, M.P. 5-DOF wireless micromanipulation using soft-magnetic core electromagnets. PhD thesis, ETH Zurich, 2010.
40. Zhang, Z.; Menq, C.H. Design and Modeling of a 3-D Magnetic Actuator for Magnetic Microbead Manipulation. *IEEE/ASME Trans. Mechatronics*, *16*.
41. Griffiths, D.J. *Introduction to electrodynamics*; Vol. 2, Cambridge University Press, 2017.
42. Khalil, W. Modeling and Control of Manipulators - Part I: Geometric and Kinematic Models. Lecture.